Enhanced seismic response prediction of critical structures via 3D regional scale physics-based earthquake simulation

Michail Korres, Fernando Lopez-caballero, Vinicius Alves Fernandes, Filippo Gatti, Zentner Irmela, François Voldoire, Didier Clouteau, David Alejandro Castro Cruz

ARTICLE TEMPLATE

Enhanced seismic response prediction of critical structures via 3D regional scale physics-based earthquake simulation

M. Korres[a,b], F. Lopez-Caballero[b], V. Alves Fernandes[a], F. Gatti[b], I. Zentner[a], F. Voldoire[a], D. Clouteau[b] and D. Castro-Cruz[b]

[a]Electricité de France-R&D Department and IMSIA UMR EDF-CNRS-CEA-ENSTA 9219, 91120 Palaiseau, France;
[b]Universite Paris-Saclay, CentraleSupelec, CNRS, MSSMat laboratory, 91190, Gif-sur-Yvette, France

ARTICLE HISTORY
Compiled November 23, 2021

ABSTRACT
Realistic physics-based 3D earthquake simulation for source-to-structure wave propagation consists of a powerful numerical tool for seismic response prediction of critical structures submitted to high safety standards. Structural response considering soil-structure interaction (SSI) is usually estimated by Finite Element Method (FEM) approach, as it is considered as the most flexible numerical approach for nonlinear structural dynamics. However, current engineering practice considers seismic input motion as vertically incident plane waves, despite the fact that this assumption excludes wave passage effects for large infrastructures and surface waves appearing from possible local basin effects. In this framework, a realistic input excitation needs to be defined as an input excitation of the FEM model, accounting for : i) a realistic dynamic excitation, ii) wave propagation path in the regional scale, and iii) local site-effects.

The Domain Reduction Method (DRM), which allows for the imposition of a 3D complex incident wave field as an input to the SSI model is adapted and examined here in a Spectral Element Method (SEM) - FEM weak coupling approach. The weak coupling is verified at first for a canonical case-study and for an increasing complexity of the dynamic excitation: i) double-couple point-source, and ii) extended fault. An optimization approach, based on the decimation of SEM output signal, is then examined in order to decrease the computational burden by maintaining the same accuracy of the final solution.

The SEM-FEM weak coupling is then used to study the SSI problem, where the impact of the reduced domain size on structural response is examined at first. The current study shows that a reduced domain of dimension greater than $4 \times \lambda_s$, where λ_s the maximum wavelength, is sufficient for a proper representation of structural response. For a fixed size model, structural and soil response are then examined for a hypothetical case-study.

KEYWORDS
domain reduction method; SEM-FEM coupling; dynamic soil-structure interaction; seismic structural analysis; paraxial elements; re-sampling/decimation;

CONTACT M. Korres Email: michail.korres@edf.fr

1. Introduction

Seismic safety of lifelines and (infra-)structures such as nuclear power plants, dams, roads, railways, and bridges are of crucial importance from an economic and social point of view. The complex interaction of these structures with the subsurface soil layers during an earthquake event represents an important phenomenon that needs to be taken into consideration so as to assess their performance. State of the art recommendations, based on recent research works, state that the seismic motion has to be controlled at the "reference bedrock" in depth, or at least at the outcropping bedrock, in order to reduce the consequences of geological conformation and site-specific parameters uncertainties, instead of the free-field motion. In such a way, the site effects can be easier analyzed separately from the analysis of the seismic hazard (*1*). To this end, the development of physics-based 3D models for the simulation of earthquake ground motion has been largely increased with the exponential increase of the computational power. In this context, important aspects of the seismic wave propagation problem can be explicitly taken into consideration, such as i) the earthquake source, ii) the propagation path, iii) the local site effects as well as iv) the non linear behavior of the soil, all gathered in a high-fidelity predictive numerical model (*2*). The latter brings an indubitable benefit to the prediction of complex scenarios, especially for the case of a near-source field (e.g. the San Francisco bay area (*3*)) and in regions of moderate seismicity where earthquake catalogs for strong ground motions are poorly populated (*4*, *5*)). As a matter of fact, current outstanding computer power endows the scientific community with the power of solving a multi-scale Soil-Structure Interaction (SSI) problem, ranging from strong ground motion prediction at a regional scale ($\sim$ several kilometers) to the prediction of the structural response at site/structure scale ($\sim$ several hundreds of meters) including details that most conventional approaches have so far neglected (source directivity, spatial variability etc, see for instance (*6*)). Several examples in the literature showcased successful end-to-end (fault-to-structure) earthquake simulations (*7–11*). However, these improvements come with a price. From a computational standpoint, the most challenging aspect is represented by the semi-infinite nature of the Earth's subsurface, which implies i) the choice of non-reflecting boundary conditions adopted at the virtual domain boundaries (*12–14*) and ii) a meshing scheme assuring *suitable* interpolation of the heterogeneous mechanical properties with their high local spatial gradients, so to grant *sufficient* numerical accuracy for the desired minimum wavelength to be rendered. Moreover, the geo-statistical uncertainty (*15*) requires, for a specific seismic scenario, a *sufficient* knowledge of the seismic source, the geological layout, and the geotechnical properties of soft sediments as those of bedrock in depth (*16*). The curse of dimensionality is easily encountered indeed: the finer the numerical modeling and the discretization, the more detailed the geotechnical, geological and seismological information required. The nonlinear material rheology of both structural components and soil deposits implies an even finer mesh to be correctly described (*2*, *14*, *17*). At the same time, a higher investment should be considered in the verification and validation (V&V) process, to increase confidence in the predictions of the simulations, for such critical decision making. (*18*)

In engineering practice, the domain at stake is represented by a small soil chunk around the structural components, usually discretized via the Finite Element Method (FEM) and solved either in the time or in the frequency domain. As far as the incident wave-field is concerned, according to Eurocode 8 (*19*) the so-called Free Field Boundary Condition (FFBC) (*20–22*) is adopted, by first defining the free-field seismic response on the outcropping bedrock (recorded or simulated) and by deconvoluting it

at the base of a horizontal soil stratification as a plane-wave motion. The deconvoluted incident wave-field is propagated through the layered soil domain up until the soil foundation (*23*).

With a similar approach, the free-field signal can be used in a Boundary Element Method - Finite Element Method (BEM-FEM) coupling framework for instance, where Green's functions for a layered visco-elastic half space are used to define the impedance matrices and the equivalent seismic forces in the BEM-FEM interface, usually placed in the vicinity of the structure (*24*). These seismic forces are then applied in a finite element (FE) framework as an excitation so as to estimate the structural response. An alternative solution in the frequency domain consists of formulating the BEM solution via the Laplace transform and evaluating the impedance operator in the time domain by a convolution integral (*25*, *26*). In this context, and in the special case where 3D physics-based simulations are used in order to define the outcropping free-field input motion, (*27*) proposed to enrich the frequency content of the seismic input motion using artificial neural networks (ANN) before calculating the dynamic impedance matrices with BEM.

All the aforementioned methodologies hardly adapt to complex site conditions (e.g. complex basin and topography effects) and seismic scenarios (near-source field directivity of a 3D incident wave field) (*14*, *20*, *28*, *29*). This drawback can be mitigated by adopting a sub-structuring approach, where the 3D excitation is obtained through wave propagation in a regional scale domain, applied as an input excitation of a smaller model on the scale of the site/structure of interest. The coupling strategy can be achieved in two alternative ways: a less intrusive *weak coupling* approach or a *strong simultaneous coupling*. The first strategy is well embodied by the so called Domain Reduction Method (DRM) (*30*), a two-step procedure where free-field ground shaking is computed via an auxiliary simulation and then injected as equivalent nodal force distribution at the bounding interface of the small-scale domain. The DRM has the advantage of an easier off-line implementation and it can take advantage of different High-Performance Computing software, tailored for seismological and structural simulations respectively, coupling Finite Difference Method (FDM) and FEM as in (*28*, *31*), FEM and FEM (*32*) and others (*33–38*). This is why this approach has been adopted here.

The strong coupling approach (*39–41*, among others) instead aims at simultaneously solving the two problems exchanging the incident and diffracted wave energy at each time step. A well known algorithm for dynamic coupling was introduced by (*42*, *43*). In this framework, (*39–41*) successfully coupled the Spectral Element Method (SEM) and the FEM, via the standard mortar approach (*44*), and for the dynamic soil-structure interaction (SSI) problem, an implementation however that adopts a sequential solution of the source-to-site wave propagation. In a similar context, (*45*) proposed FDM-FEM coupling. The core idea of the strong coupling to enforce the continuity of the solution at the interface, producing a real time exchange of information between the coupled models, leads to a definition of the 3D input excitation on the boundary of the finite element domain used in order to perform the dynamic SSI analysis that is the exact solution of the problem. This is the main difference with weak coupling techniques that only account for the complex incident motion without accounting for the diffracted waves (*30*, *46*). In addition, in the strong coupling and given that each problem is solved simultaneously on the interface in general no need for absorbing boundary is necessary. In this framework, the size of the FEM domain can in principle be reduced at the soil-structure interface and only depends on the computational capacity of each methodology and as a result on the discretization

of each domain. On the contrary, in a weak coupling approach the accuracy of the response is related to the size of the finite element domain as a result of the position of the absorbing boundary condition. Nevertheless, two major drawbacks of these strong coupling techniques are: i) the difficulty of the implementation in existing codes due to their intrusive character, and ii) the performance of the implemented solution on a High Performance Computing (HPC) framework, which are the main reasons why these types of solutions are not examined in this work.

Regardless the coupling scheme, the choice of the two numerical methods to be coupled depends on the scale of the problem (regional or site/structure) and on the rheology of the soil media (linear, nonlinear). In this regard, the FEM is traditionally well suited for structural elements and nonlinear behavior to be taken into account for the soil-structure interaction (SSI) problem (*2*). More recently, the FEM has been used in a large-scale domain earthquake simulation, due to its flexibility (*47–50*). Another advantageous solution to solve regional scale numerical wave propagation is the SEM (*2*, *5*, *51*, *52*), belonging to the FEM family, with higher order polynomials as basis functions. The SEM displays a lower numerical dispersion (*53*, *54*), compared to the FDM (traditionally employed in seismology), as quoted by many authors for many decades, e.g. (*55*). (*56*) proposed in the SEM context the use of Lagrange polynomials in conjunction with the Gauss-Lobatto-Legendre (GLL) quadrature, which leads to a diagonal mass matrix of the problem, allowing a faster solution of the system of equations. This diagonal matrix, in conjunction with the higher order shape functions allowing the choice of larger elements for the discretization of the physical domain in comparison to the FEM methodology.

The aim of this work is to apply the DRM method by employing a SEM kernel to solve the auxiliary wave propagation problem and a FEM kernel for the reduced domain problem. Compared to other implementations of the DRM strategy ((*29*, *57–59*) among others), the aim of the present work is two-fold and it resides in: i) the optimization of the transferred field between SEM-FEM in order to accelerate the source-to-structure wave propagation computation, and ii) the use of the *paraxial boundary conditions* (*60*, *61*) to both absorb outgoing waves impinging the fictive boundary and to apply the dynamic excitation (formulation proposed by (*62*)) on the reduced scale domain.

This paper is organised as follows: Section 2 focuses on a brief description of the DRM theory and of the paraxial element formulation used to reconstruct the dynamic excitation on the boundary of the reduced domain. Paraxial elements consist of a surface boundary condition and allow a simple and robust implementation while their consideration on the DRM framework lies in the fact that they provide a smaller computational domain comparing to other DRM applications where absorbing layers are taken into account ((*29*, *57–59*, *63*) among others). Sub-section 2.3 focuses on the description of the adopted SEM/FEM weak coupling approach and discusses spatial and temporal discretisation hypothesis used to optimize the weak coupling. Finally, the numerical verification of the coupling approach will be presented on section 3, and for a canonical case-study proposed in the literature. Applications on the SSI problem will be discussed in section 4 in order to identify the importance of a realistic input excitation definition.

2. SEM-FEM Numerical modeling

The key concept of the DRM approach lies in the use of a complex incident wave field to be imposed as an input excitation to the SSI model (*14*, *64*). In this context, the objective of the DRM is to transfer the dynamic excitation of the seismic source closer to the boundaries of a reduced (smaller) domain of interest, at the scale of the site/structure.
The initial domain of interest Ω, is divided in two sub-domains by a virtual boundary surface Γ: i) the interior domain Ω_s, and ii) the exterior domain Ω'_s (Fig 1a). The wave propagation problem is then solved in two separate steps:

(1) **Auxiliary domain problem** $\mathcal{P}_0$: it consists of a source-to-site simulation on a background soil configuration Ω^0_s, where local features (eg. geological aspects, structures, etc) of interest in Ω_s are replaced with a simpler soil domain modeling as the one adopted for the soil in depth, see (Fig. 1b). Coarser discretization can be chosen, based on a higher wave velocity of the soil media (soil in depth assimilated to rock) and the whole calculation is performed only once for the specified earthquake source and regional scale properties, so as to define the corresponding ground motion at the boundary of the interior domain;
(2) **Reduced domain problem** $\mathcal{P}_r$: The second step considers the interior domain where the local features of interest are accurately modeled (see Fig. 1c). The input excitation expressed in terms of equivalent nodal forces obtained directly from $\mathcal{P}_0$ and applied on the boundary Γ in a region that is slightly bigger than the local interior domain. The soil outside the boundary Γ is only used for absorbing the diffracted waves traveling out of the domain and incompatible with $\mathcal{P}_0$ solution. In this case, for any change of system parameters inside the localized region of interest (interior and exterior domains), only this step has to be repeated so as to determine the variation of the wave propagation inside the interior domain.

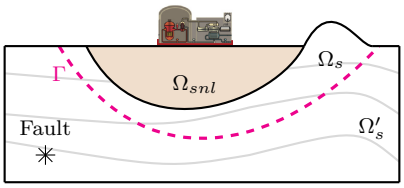

(a) Problem of reference.

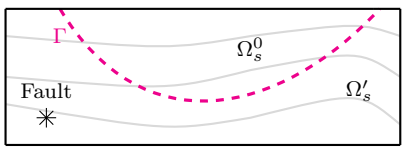

(b) Auxiliary domain problem.

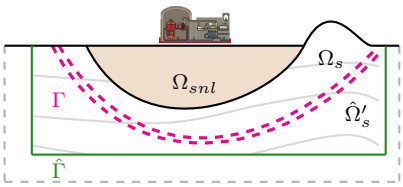

(c) Reduced domain problem.

Figure 1.: Schematic representation of the domain reduction method (adopted from (*30*)).

Finally, it is important to remind here that in the DRM approach proposed by (*30*), two key points must be treated: i) an external region with a suitable absorbing

boundary condition around the reduced domain, and ii) the definition of the equivalent nodal forces on a region in the reduced domain boundary.

Concerning the former point, alternative approaches for suitable absorbing boundary conditions with the DRM methodology have been proposed in the literature: simple dash-pot approach (e.g. *34*, *36*, *65*, *66*), buffer zones or damping layers (e.g. *8*, *9*, *30*, *38*, *46*, *67*), PML (*57*, *68*, among others). In the following (subsection 2.1), the adopted solution in this work for the boundary condition (*i.e.* paraxial approximation) will be briefly presented.

As far as the latter point is concerned, a DRM layer needs to be defined for the computation of the equivalent nodal forces. The way that these equivalent nodal forces are computed and implemented in the current weak SEM-FEM coupling is presented in subsection 2.3.

2.1. *Paraxial Boundary Conditions*

The seismic excitation from the auxiliary domain problem is then transferred (in terms of equivalent nodal forces (*12*, *30*, *69*)) as an input excitation on the reduced domain problem on the scale of the site/structure to be studied with the FEM (*70*) open-source software. The weak coupling SEM3D-Code_Aster is ensured by the *paraxial elements*, capable to impose the dynamic excitation (*62*, *70*) as well as to absorb the outgoing waves arriving on the boundary. The formulation of the paraxial elements was initially introduced by (*61*) and (*60*) while the implemented version in Code_Aster is based on a modification initially discussed by (*62*) allowing to take into account the dynamic excitation. Starting from the general expression of the elastic equation of motion, the derivation of the spectral impedance on the boundary of the reduced domain Γ requires the projection of the equation of motion on a local tangent plane $(\mathbf{e}_1, \mathbf{e}_2)$, with outward normal $\mathbf{e}_3$. The solution of this projected equation, expressed in the Fourier wave number-frequency domain, $\hat{\mathbf{u}}'$ and $\hat{\mathbf{u}}_3$, leads to the derivation of the spectral impedance on the interface Γ, provided schematically with Eq. 2.1 .

$$\hat{\mathbf{t}}(\boldsymbol{\xi}, \mathbf{x}_3 = 0, \omega) = a_0 \mathbf{e}_3 + b_0 \boldsymbol{\xi} + c_0 \boldsymbol{\xi} \times \mathbf{e}_3 \tag{2.1}$$

where $a_0, b_0,$ and c_0 are functions of the wave number vector $\boldsymbol{\xi}$ associated with the local plane coordinate $\mathbf{x}'$ and the pulsation ω. In order to obtain the expression of Eq. 2.1 in the physical domain, an inverse Fourier transform has to be applied.

$$\hat{\mathbf{t}}(\mathbf{x}', \mathbf{x}_3 = 0, t) = \int_{-\infty}^{+\infty} \int_{-\infty}^{+\infty} \hat{\mathbf{t}}(\boldsymbol{\xi}, \mathbf{x}_3 = 0, \omega) e^{-i(\omega t + \boldsymbol{\xi} \cdot \mathbf{x}')} d\omega d\boldsymbol{\xi} \tag{2.2}$$

Eq. 2.2 is not local in time and space. In addition, the computation of the double integral in Eq. 2.2 cannot be conveniently obtained for the general case of a complex geological domain and 3D excitation. In order to simplify the computation of the impedance, (*60*, *61*) proposed to develop the wave numbers for the transverse ξ_s and longitudinal wave ξ_P as a function of the ratio κ.

$$\begin{aligned} \xi_P &= \tfrac{\omega}{C_P} \sqrt{1 - C_P^2 \kappa^2} \\ \xi_S &= \tfrac{\omega}{C_S} \sqrt{1 - C_S^2 \kappa^2} \end{aligned} \qquad \text{where } \kappa = \tfrac{|\boldsymbol{\xi}|}{\omega} \tag{2.3}$$

where, C_S, and C_P are the shear and longitudinal wave velocity respectively, under the assumption of linear isotropic elasticity. The wave vectors ξ_S and ξ_P, can now be approximated through a Taylor expansion in the form of :

$$\xi_a = \frac{\omega}{C_a}\sqrt{1 - C_a^2\kappa^2} \approx \frac{\omega}{C_a}\left[1 - \frac{1}{2}C_a^2\kappa^2 + ...\right] \quad a = S, P \tag{2.4}$$

The paraxial approximation of the impedance consists in assuming that the ratio κ is sufficiently small ($\kappa \ll 1$), and thus the lower orders of the Taylor expansion are enough for the approximation of the values of ξ_S and ξ_P.
It is important to state here that this assumption of $\kappa \ll 1$, is valid for large frequencies ω, or small ξ (propagation in the direction close to $\mathbf{e}_3$). More precisely, based on Eq. 2.3, the wave vectors ξ_S and ξ_P take imaginary values (evanescent waves) for $|C_S\kappa| > 1$, and thus stability problems appear in the solution. An easy modification that allows to eliminate the evanescent component of the solution is based on the restriction of the range of solutions to those waves that propagate within a cone of the $\mathbf{e}_3$ vector (paraxial waves).

Here, the zero-order paraxial approximation is used in Code_Aster (*70*). Consequently, the expression of the spectral impedance (Eq. 2.1) can be rewritten in the schematic form of Eq. 2.5, that can be assimilated to a distribution of linear viscous dash-pots:

$$\boldsymbol{t}(\boldsymbol{x}', x_3 = 0, t) = A_0(\partial_t \mathbf{u}) \tag{2.5}$$

where, A_0 is a function of C_S, and C_P representing the shear and longitudinal wave velocity.

Finally, it is well-known that the accuracy of the paraxial approximation could diminish significantly due to soil material heterogeneity, the increased wave-field complexity, and the angle of incidence of the arriving scattered wave field among others. Consequently, it is clear that when a more complex diffracted wave field with an angle of incidence far from the vertical one (*e.g.* surface waves, wave scattering) arrives on the boundary, the zero-order approximation present low absorbing performance (*60*, *61*). This phenomenon that might impact the size of the finite domain to be numerically modeled for the SSI problem is discussed in subsection 4.1. n order to amend for this inconvenience, (*60*, *61*) proposed higher-order approximations in order to increase the performance of the boundary for higher incidence angles. In a similar way, higher-order approximations were used by (*71*) in order to account for material heterogeneity. These solutions however, increase the complexity of the numerical implementation (involvement of higher-order derivatives of the traction vector on the boundary) and might cause stability problems.

2.2. *Variational formulation of the coupling*

The variational formulation of the coupling is derived here in order to provide the expression of the external dynamic excitation. On the boundary surface of the reduced domain Γ, a continuity of the displacement and traction vector needs to be considered in order to ensure the equilibrium on the interface (Eq. 2.6).

$$\begin{aligned} \mathbf{u}_s - \mathbf{u}'_\mathbf{s} &= 0 \\ \mathbf{t}_s + \mathbf{t}'_s(\mathbf{u}'_s) &= 0 \end{aligned} \tag{2.6}$$

Based on the *Sommerfeld* radiation condition, the incident wave field $\mathbf{u}'_i$ has to be equal to the total wave field $\mathbf{u}'_s$ in infinity. Consequently, the diffracted wave field $\mathbf{u}'_r$ can be expressed following Eq. 2.7.

$$\begin{aligned} \mathbf{u}'_s &= \mathbf{u}'_i + \mathbf{u}'_r \\ \lim_{r\to\infty} \|\mathbf{u}'_r\| &= 0 \end{aligned} \tag{2.7}$$

The diffracted field $\mathbf{u}'_r$, can now be completely described via the zero-order paraxial approximation and as a result the traction vector takes the following form.

$$\begin{aligned} \mathbf{t}_s = -\mathbf{t}'_s(\mathbf{u}'_s) = -\mathbf{t}'_s(\mathbf{u}'_i) - \mathbf{t}'_s(\mathbf{u}'_r) \approx -\mathbf{t}'_s(\mathbf{u}'_i) - A_0(\partial_t \mathbf{u}'_r) \Rightarrow \\ \mathbf{t}_s \approx -\mathbf{t}'_s(\mathbf{u}'_i) - A_0(\partial_t \mathbf{u}'_s) + A_0(\partial_t \mathbf{u}'_i) \end{aligned} \tag{2.8}$$

Finally, the variational formulation of the system can be expressed based on the expression of the traction vector.

$$\int_{\Omega_s} \rho \partial_{tt} \mathbf{u}'_s \cdot \mathbf{w} d\Omega + \int_{\Omega_s} \boldsymbol{\sigma}'_s : \boldsymbol{\epsilon}(\mathbf{w}) d\Omega + \int_{\Gamma} A_0(\partial_t \mathbf{u}'_s) \cdot \mathbf{w} d\Gamma = \int_{\Gamma} (-\mathbf{t}'_s(\mathbf{u}'_i) + A_0(\partial_t \mathbf{u}'_i)) \cdot \mathbf{w} d\Gamma \tag{2.9}$$

External forces representing the dynamic excitation are described from the right-hand side of Eq. 2.9 from where it is clear that in order to "transfer" the excitation of the fault close to the domain of interest, only the traction vector $\mathbf{t}'_s(\mathbf{u}'_i)$, and the viscous stress vector field from the incoming velocity $A_0(\partial_t \mathbf{u}'_i)$ are required. This conclusion is of crucial importance as it demonstrates which are the necessary fields to be transferred from SEM to FEM in order to ensure the coupling.

2.3. *Coupling procedure and comparison methodology*

The traction vector $\mathbf{t}'_s(\mathbf{u}'_i)$ and the incident wave velocity field $\dot{\mathbf{u}}'_i$, are the necessary fields needed in order to correctly construct the transient dynamic impedance with the paraxial elements on the boundary Γ of the reduced domain. Nevertheless, special care needs to be taken in the definition of this traction vector for each one of the numerical solutions.

Kinematic fields such as displacement and velocity, are discrete fields directly obtained as the solution of the numerical time integration scheme in each one of the two computational software. On the contrary, the traction vector, is obtained after a post-processing procedure, which is fundamentally different between SEM and FEM, due to their differences in terms of formulation (shape functions, quadrature rules and degrees of freedom-dofs). In consequence, the approximation introduced from a direct transfer of a traction vector on the boundary of the reduced domain might lead to important errors in the definition of the dynamic excitation.

A remedy to this approximation, consists in reconstructing the traction vector on a FEM framework, based on the more accurate expression of the displacement fields directly obtained as the solution of the wave propagation problem in SEM3D.

Consequently, the necessary kinematic fields to be "transferred" between the two software are : i) the displacement field $\mathbf{u}$, exported in an auxiliary layer neighboring to the reduced domain boundary so as to reconstruct the traction vector in a FEM

framework, and ii) the velocity field $\dot{\mathbf{u}}$ exported on the reduced domain boundary (Fig. 2).

A schematic representation of the coupling between SEM and FEM is presented in Fig. 2 and the procedure of field transfer is executed as follows:

(1) Define the surface boundary of the DRM interface and the neighboring auxiliary layer in SEM domain (Fig. 2a).
(2) Export displacement and velocity fields $(\mathbf{u}, \dot{\mathbf{u}})$ on predefined sensor points on GLL points lying on the DRM boundary and auxiliary layer. These points are the nodes of the FEM mesh and the kinematic fields are obtained using the high order basis functions of SEM. No spatial interpolation is therefore needed at this interface, since a matching correspondence between SEM and FEM dofs is enforced.
(3) On the auxiliary layer (Fig. 2b), impose nodal displacement field $\mathbf{u}$ and compute the traction vector solving the static problem with FEM. The traction vector defined on nodes is simply the nodal forces.
(4) In the reduced domain (Fig. 2c), reconstruct the dynamic excitation from using the velocity field $\dot{\mathbf{u}}$ directly exported from SEM, and the nodal forces F_{node} computed in FEM from the auxiliary layer model.

All field transfer between the SEM and FEM codes was performed using MEDCoupling, an open-source SALOME[1] tool used for mesh/field handling (*72*).

It is important to state here that the proposed methodology for the computation of the traction vector is based on the assumption of hexahedral 8-node linear elements within the FEM. One of the main advantages of the finite element method lies in the fact that quadratic elements as 10-node tetrahedral ones can be used in the numerical model so as to represent any more complex geometries as well as decrease the number of points per wavelength for a correct wave propagation. In this framework, the proposed methodology for the traction vector calculation has to be adapted to a reduced domain discretized with quadratic tetrahedral elements between step 3 and 4 of the coupling procedure.

As already discussed in the introduction, the difference of the proposed methodology, comparing to the one proposed by several authors in the literature ((*29*, *57–59*, *63*) among others) lies in the fact that the dynamic excitation is imposed directly on the boundary of the reduced domain. This provides an important advantage deriving from the use of the paraxial elements. In this context no extra absorbing soil layers are needed so as to absorb outgoing waves and as a result the size of the FEM domain to model is less important.

2.4. *Strategy for the spatial and temporal discretization of the problem*

The main hypothesis for the spatial and time discretization of the finite element model are presented hereafter. The presented assumptions are to be considered later in the numerical verification of the SEM-FEM coupling approach as well as in the numerical applications on the SSI problem.

[1] https://www.salome-platform.org/

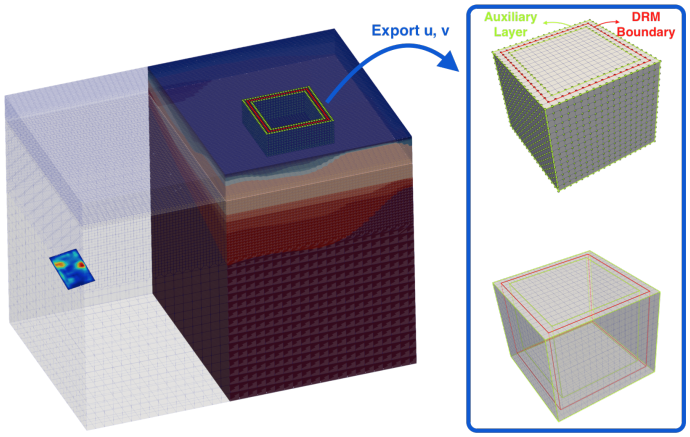

(a) Regional domain in SEM3D and zoom on the reduced domain.

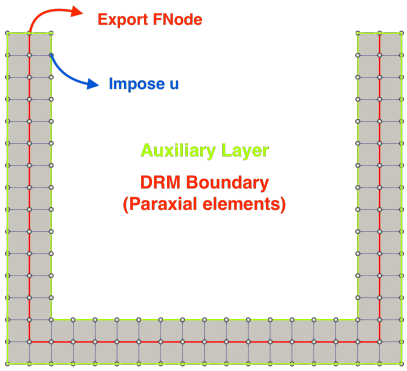

(b) Auxiliary layer: computation of nodal forces in FEM.

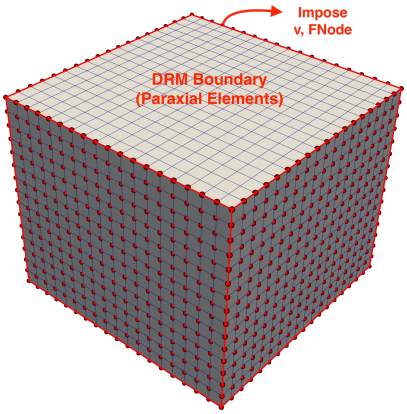

(c) Reduced domain.

Figure 2.: Schematic representation of the coupling procedure between SEM3D and code_aster.

2.4.1. Spatial discretization

According to (*5*, *73*, *74*), seismic wave propagation with the SEM can be accurately modeled when a number of N = 5 points per wavelength (or equivalently a 4^{th} order GLL approximation) is adopted for the spectral elements. Based on this assumption, the maximum size of the spectral elements on the basin, and the minimum shear wave velocity, the maximum frequency of the spectral element model can be estimated.

Element size for the FEM model is defined based on this maximum frequency of the SEM model. In a similar way as with the SEM, in FEM the empirical rule says that 10 points per wavelength are sufficient when linear elastic finite elements are used (*75*). As a result, the element size in FEM can be fixed at $\Delta x_{FEM} = \frac{V_S^{min}}{10 \times f_{max}}$. This size corresponds to the spacing between the sensor points introduced in SEM3D in order to export the necessary kinematic fields. As explained in the description of the coupling procedure, the kinematic fields are exported directly on the sensor points after an interpolation inside SEM taking into advantage the high order basis functions of the spectral element method.

In a similar SEM-FEM weak coupling approach, (*76*) stated that a ratio of 1/8 between the FE (Δx_{FEM}) and the SE element size is sufficient for a 4^{th} order GLL approximation. Nevertheless in this study we stick to a ratio of 1/10 in order to satisfy the assumption of 10 points per wavelength.

2.4.2. Time discretization

An explicit 2^{nd} order (*leap-frog*) time-integration scheme (*13*) is used for the numerical time-integration in SEM3D, while an average constant acceleration implicit scheme is considered in the finite element context with (*77*). One of the major difficulties when coupling explicit and implicit time-integration schemes lies in the difference of the computational time-step. In the explicit scheme smaller time-steps are usually necessary so as to ensure the stability of the time-integration scheme. This is not the case for the average constant acceleration implicit scheme which is unconditionally stable and thus larger time-steps can be chosen (without excess, to avoid a too large period distortion).

In this framework, an optimization procedure is proposed here in order to increase the efficiency of the coupling procedure in terms of computational time and memory demand. This optimization consists of a re-sampling/decimation procedure to be applied to the initial signal exported from SEM before introducing it to the finite element computation. As already explained, the main goal is to obtain a larger time-step in the implicit solver than the one of the explicit one.

In the decimation/downsampling procedure in digital signal processing (DSP) the Nyquist frequency, f_{NQ}, plays a crucial role in aliasing effect. More specifically, any frequency component above the Nyquist frequency will cause aliasing of the final signal. In order to avoid aliasing special anti-aliasing filters need to be applied before re-sampling the signal.

The re-sampling steps are summarized as following:

(1) **Define the maximum frequency f_{max} of the problem** :
The f_{max} is the frequency that the spectral element code can propagate for a given order of GLL approximation and mesh discretisation (section 2.4.1).

(2) **Define the Nyquist frequency f_{NQ}**:
The Nyquist f_{NQ} (or cut-off frequency) is considered close to the maximum frequency of the problem. The Nyquist frequency is to be defined prior to the filtering.

(3) **Apply the anti-aliasing filter**:
Low-pass filter the kinematic fields for the value of f_{NQ}. The filter used in all of the presented cases is an order 8 Chebyshev type I filter.

(4) **Define the new sampling frequency f_S**:
Compute $f_S = 2 \times f_{NQ}$.

(5) **Define the new time-step of the input signal Δt_{CA}^{input}**:
Compute $\Delta t_{CA}^{input} = \frac{1}{f_S}$

It is important to clarify at this level that the Δt_{CA}^{input} of the input signal should not be confused with the time-step of the FEM computation. Even if the time integration is implicit in the FE solution, for reasons of accuracy a smaller time-step $\Delta t_{implicit}$ is to be considered for the computation. A flow-chart of the aforementioned approach is given in the Fig. 3.

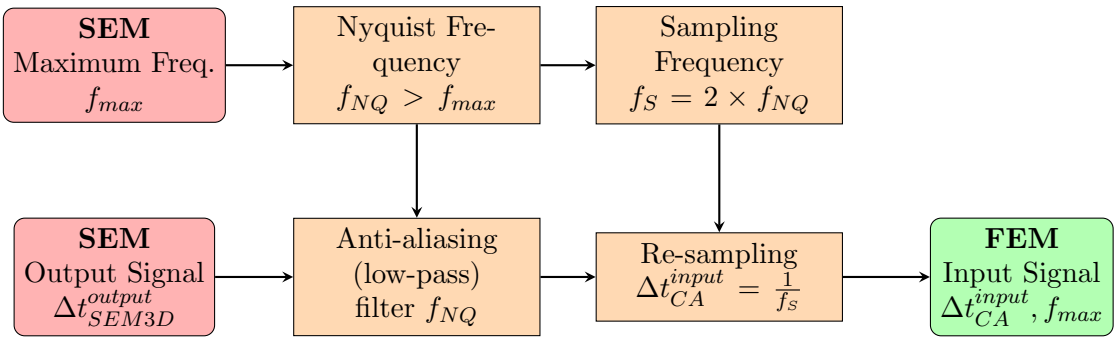

Figure 3.: Optimization procedure of the FEM input signal.

2.5. *Comparison procedure: Goodness-of-fit (GOF) criteria*

In order to compare the obtained solution with a solution of reference, efficient comparison criteria taking into account phase as well as amplitude errors should be considered. The current evaluation of numerical results is based here on the use of the goodness-of-fit criteria (GOF) proposed by (*78*, *79*). The main advantages of these approaches is based on the time-frequency representation (TFR) of the seismic signal, which is obtained after a continuous wavelet transformation. In this context, the evolution of the frequency content of the signal with respect to time can be easily represented and thus local time-frequency differences can be identified. Based on the aforementioned, a single value goodness-of-fit (GOF) criterion, can be defined for the envelope and the phase of the signals to be compared. This single value GOF criterion will be used here so as to evaluate the solution obtained from the coupling approach. For the sake of simplicity, the expression of the GOF for the envelope and phase criteria is briefly provided here. For more information concerning alternative comparisons and a more detailed description of the theoretical background of the comparison methods, the reader should refer to (*78*, *79*).

The local time-frequency (TF) envelope and phase difference can be defined from Eq. 2.10 as follows :

$$\begin{aligned} \Delta E(t,f) &= |W(t,f)| - |W_{REF}(t,f)| \\ \Delta P(t,f) &= |W_{REF}(t,f)| \frac{\{Arg[W(t,f)] - Arg[W_{REF}(t,f)]\}}{\pi} \end{aligned} \tag{2.10}$$

where $W(t,f)$, and $W_{REF}(t,f)$ are the continuous wavelet transforms (TFR) of the signal to be evaluated and the signal of reference respectively.

Based on these TFR the single value misfit criteria for the envelope and the phase are obtained from Eq. 2.11 :

$$\begin{aligned} EM &= \sqrt{\frac{\Sigma_f \Sigma_t |\Delta E(t,f)|^2}{\Sigma_f \Sigma_t |W_{REF}(t,f)|^2}} \\ PM &= \sqrt{\frac{\Sigma_f \Sigma_t |\Delta P(t,f)|^2}{\Sigma_f \Sigma_t |W_{REF}(t,f)|^2}} \end{aligned} \tag{2.11}$$

Finally, based on these misfit-single value criteria, the GOF can be defined by Eq. 2.12:

$$\begin{aligned} EG &= A\exp\{-|EM|^k\} \\ & \qquad \text{where } A>0, \quad k>0 \\ PG &= A\exp\{-|PM|^k\} \end{aligned} \tag{2.12}$$

where A is a parameter that quantifies the correspondence between the signal of reference and the computed one and k determines the sensitivity of the GOF value. For the specific case of $A = 10$ and $k = 1$ the criterion is similar to the formula proposed by (*80*). The result provided from this comparison is a score in the scale of 0 to 10 allowing to evaluate the similarity of the two signals: i) for a value of 0 there is no correspondence between the two signals while for a value of 10 a perfect correspondence can be observed.

Finally, according to (*80*), based on the GOF score, the correspondence between the two signals can be verbally quantified as presented in Table 1:

Table 1.: Verbal representation of the discrete GOF score (adapted from (*80*))

Goodness-of-Fit	
Verbal Value	**Numerical Value**
Excellent	8 - 10
Good	6 - 8
Fair	4 - 6
Poor	0 - 4

3. Numerical verification for a canonical case-study

For the numerical verification of the coupling procedure, the auxiliary domain problem (Fig. 1b) is considered identical to the initial problem of reference (Fig. 1a). In this context, the equivalent nodal forces correspond to the exact solution of the seismic wave propagation problem and their application on the reduced domain should generate a soil response, in the reduced domain, that is identical to the one obtained from the problem of reference. Numerical verification is provided here for the canonical case of CAN4 (*81*, *82*), and the coupling is verified for an increasing complexity of the dynamic excitation source in order to evaluate the efficiency of the proposed approach.

3.1. *Description of the numerical model*

The geometry of the case-study to be modeled numerically in SEM3D is given in Fig. 4. It consists of a $22 \times 12 \times 6$ km^3 soil domain with a trapezoidal basin on the surface.

In SEM3D, 11,800 spectral elements are used to model the problem, with five Gauss-Lobatto-Legendre (GLL) points in each direction of the element. The minimum element size is of $40 \times 40 \times 15$ m^3 on the surface, and inside the trapezoidal basin. The reduced domain (DRM) consists of a $200 \times 200 \times 110$ m^3 box represented with 78,700 finite elements. The center of the DRM domain is positioned in the beginning of the axis O (0.0, 0.0, 0.0) m (red box in Fig. 4).

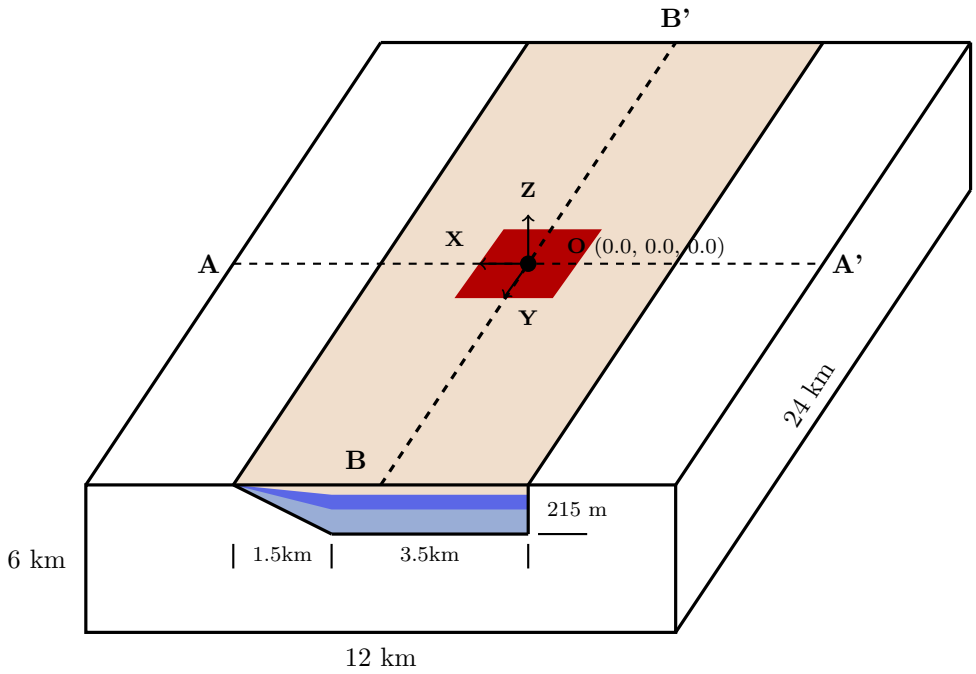

Figure 4.: Canonical case-study CAN4.

Mechanical properties of the numerical SEM3D model are given in Table 2. For the numerical verification purpose, no damping is considered in the numerical model.

Table 2.: Mechanical properties of the numerical model.

	Thickness at O (0, 0, 0)	**C_S [m/s]**	**C_P [m/s]**	**ρ [kg/m^3]**
Soil	15.8	400	1100	1800
	47.4	500	1400	2100
	142.4	650	2500	2200
Rock	5785	2600	4500	2600

3.1.1. Dynamic excitation and absorbing boundary conditions

Perfectly Matched Layers (PML) (*83*), is the adopted absorbing boundary condition ensuring the absorption of spurious waves arriving on the outer boundary of the SEM3D domain.

The dynamic excitation within the SEM3D domain will be introduced based on two different types of source models: i) a double-couple point-source, and ii) an extended fault excitation (*84*).

The first type of dynamic excitation used in SEM3D is the one proposed in the canonical case of CAN4 (*82*). It consists of a double-couple point-source excitation with a strike of 22.5^o, dip of 90.0^o, and rake of 0.0^o. The seismic moment of the source is reduced to $M_0 = 8.7 \cdot 10^{15}$ N.m from the initial value in order to have a lower magnitude earthquake and the moment time history is presented with Fig. 5. The hypocenter of the point source is located at (50 m , 0 m, -3000 m).

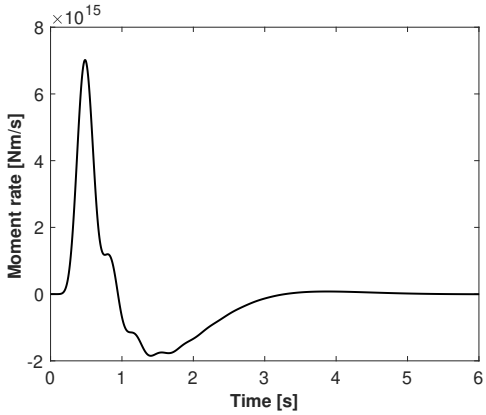

Figure 5.: Moment time history for the point-source (see also CAN4 and (*82*)).

Concerning the second verification model, the extended fault of 3×3.5 km has a Strike of 180^o, Dip of 7.8^o, Rake of -179^o and its hypocenter is located at (2164 m, 0 m, -1772 m) (Fig. 6a). Total seismic moment of the extended fault is equivalent to $M_0 = 4.63 \cdot 10^{15}$ N.m ($M_w \approx 4.4$). The time distribution of the seismic moment M_0 based on the position of different sub-sources of the fault is given with Fig. 6b. The maximum slip generated from the fault is around 0.06 m and the slip distribution along with the triggering time are given in Fig. 6c, while the source time function is provided in Fig. 6d. The rupture process of this kinematic source is based on a waveform inversion procedure with the empirical Green function (EGF) as described in (*84*).

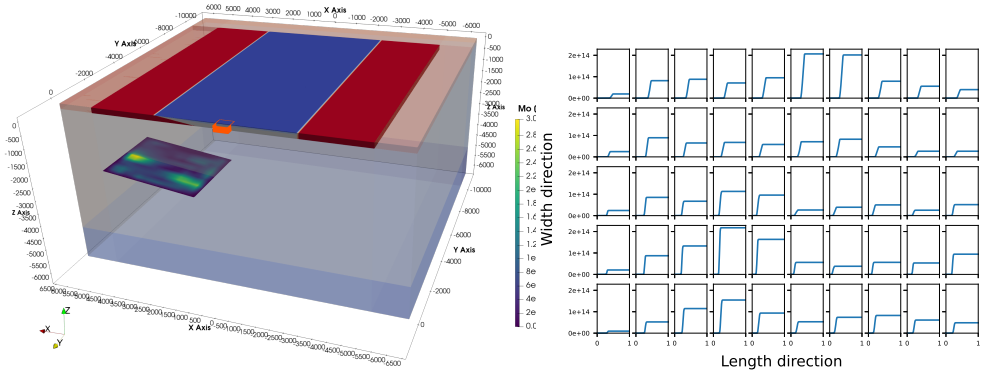

(a) Topography of the SEM3D model (A-A' cut from Fig. 4).

(b) Mo vs Time for different positions on the source.

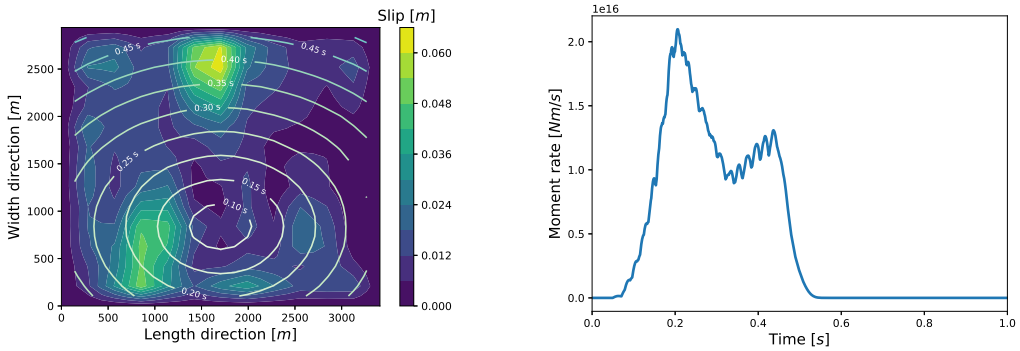

(c) Slip distribution and triggering time.

(d) Source time function.

Figure 6.: Description of the extended fault excitation in the SEM domain.

3.2. *No re-sampling approach*

The numerical verification of the SEM-FEM weak coupling is provided at first and for the unprocessed SEM3D output ($\Delta^{output}_{SEM3D} = 0.002$s) where the proposed optimization procedure (re-sampling) is not adopted for the exported kinematic fields. The goal of this part is to numerically verify the coupling approach by a direct injection of the "recorded" signal obtained from SEM3D. Following the coupling description discussed in subsection 2.4 and based on the mechanical properties of the soil domain (Table 2) spatial and time discretization of the SEM and FEM numerical models are gathered in Table 3.

Table 3.: Spatial and temporal discretization - *No re-sampling*.

Model Parameters	
V_S^{min} [m / s]	400
Element size FEM [m]	$4 \times 4 \times 4$
Nb Nodes (Interface)	$4 \times 4 \times 4$
Maximum targeted freq. [Hz]	10
Time-step output signal (SEM3D) [s]	0.002
Nyquist freq. [Hz]	250
Sampling freq. [Hz]	500
Time-step input signal (FEM) [s]	0.002
Time-step computation (FEM) [s]	0.002

Based on the value of $f_{max} = 10$ Hz, the output signals at surface from both models are band-pass filtered between 0.1 - 10 Hz. Comparison of the numerical results is provided according to the iso-surface of the GOF score of the criteria of (*78*) presented in Fig. 7. According to this Fig. 7, the GOF score is equal to almost 10 everywhere in the soil surface of the reduced domain. Similar results are observed for both types of excitation source, however only the extended fault excitation is presented in Fig. 7 and for reasons of brevity. Consequently, a good agreement is considered between the full-SEM3D response and the one from the DRM solution (see also Table 1).

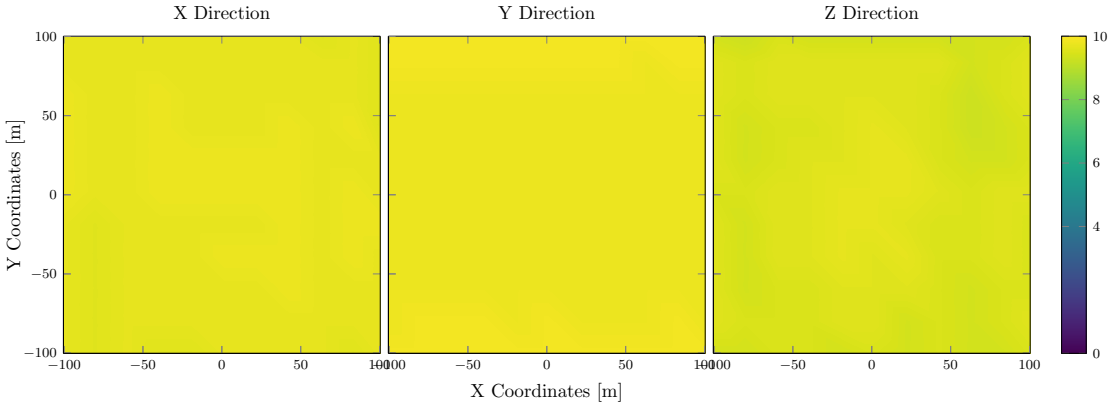

Figure 7.: Iso-surface of the GOF criteria for the extended fault excitation and on the soil surface of the reduced domain.

Finally, numerical results are also compared in terms of acceleration time-histories (Fig. 8) for several points at the surface of the reduced domain and along the BB' cut in Fig. 4. Similar to the conclusions obtained from the GOF score on the surface, this figure also shows a good agreement between the full-SEM3D simulation, denoted as "SEM3D" in Fig. 8, and the SEM-FEM coupled solution denoted as "DRM" on the same figure.

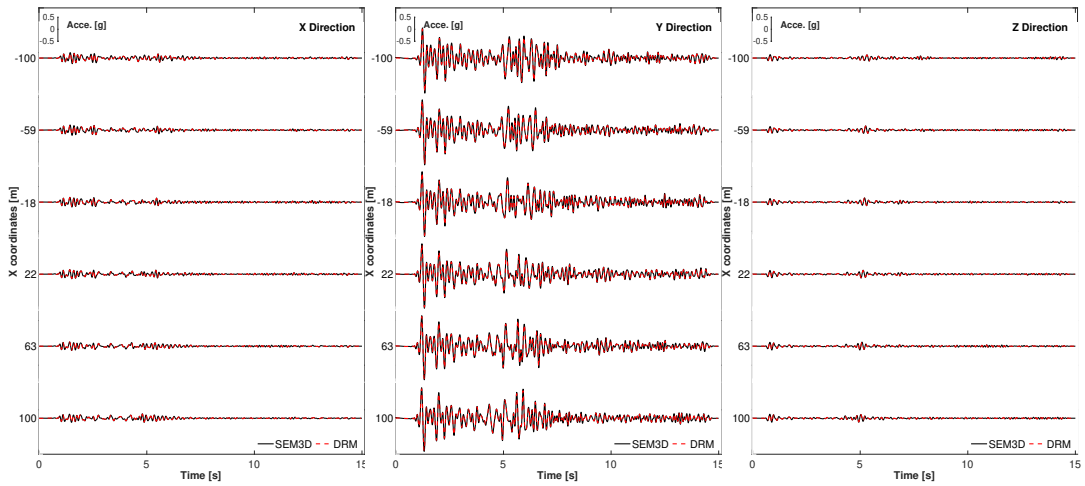

Figure 8.: Comparison of the acceleration time-histories between the "SEM3D"' solution and the "DRM" approach: X (left), Y (center), and Z (right) component.

3.3. *Optimization approach: re-sampling of the input signal*

Following the analysis described in subsection 2.4, the optimization of the transfer of kinematics fields is adopted here. A parametric study on the Nyquist frequency definition is considered at first so as to evaluate the impact of this value on the accuracy of the coupling results. Five different cases are considered and summarized in Table 4 for both types of excitation source.

Table 4.: Spatial and temporal discretization - *re-sampling approach*.

Starting Parameters					
V_S^{min} [m / s]	400				
Element size FEM [m]	$4 \times 4 \times 4$				
Maximum targeted freq. [Hz]	10				
Time-step output signal (SEM3D) [s]	0.002				
Cases	**1**	**2**	**3**	**4**	**5**
Nyquist freq. [Hz]	250	40	20	15	12.5
Sampling freq. [Hz]	500	80	40	30	25
Time-step input signal (FEM) [s]	0.002	0.012	0.024	0.032	0.04
Time-step FEM computation (FEM) [s]	0.002	0.002	0.002	0.002	0.002

For each one of the five cases, the re-sampled input signal is compared to the initial one (before re-sampling/obtained from SEM3D), in terms of GOF score. Comparison is provided everywhere on the boundary of the reduced domain and for the Y component of the displacement, velocity which are the kinematic fields of interest (see also section 2.3). For the sake of brevity, only the case of the extended fault is presented hereafter. The score on the lateral boundaries is "flattened" and plotted on the same plane as the base of the reduced domain, in order to provide an easier visual presentation. For values of GOF < 9 the same color (gray) is used to represent each point (Fig. 9).

Based on the values of the GOF score (Fig. 9), the impact of the re-sampling process is more important for the velocity field, and practically vanishing for the displacement field, where higher scores are observed. In addition, according to the same Fig. 9 as the Nyquist frequency approaches the value of the maximum frequency of the problem ($F_{NQ} = 40 \rightarrow 12.5$Hz), the lower is the score of the GOF criteria. This effect is related to the low-pass filter applied before the re-sampling as the cut-off frequency of the low-pass filter (or equivalently the Nyquist frequency) does not consist of an exact limit value for the activation of the filter.

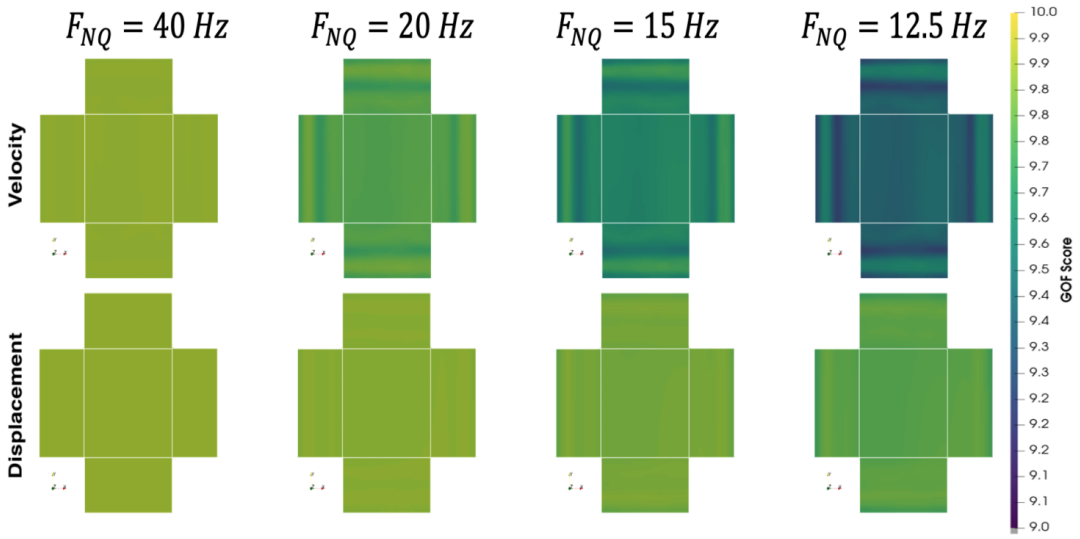

Figure 9.: Score of the GOF criteria on the boundaries of the reduced domain for the Y component. Comparison between the signal or reference (SEM3D) and the re-sampled one. Lateral sides of the reduced domain are flattened on the plane of the base.

Naturally, the same Nyquist frequency should provide a higher score of the GOF criteria for a smaller range of frequencies of interest (0.1 - 8 Hz for example). Fig. 10 shows the score of the GOF criteria based on the position along the AA' line (see also Fig. 4) on the surface of the reduced domain, and for the five different cases of Table 4. Two different values of f_{max} are considered for the current case: i) $f_{max} = 10$ Hz in Fig. 10a, and ii) $f_{max} = 6$ Hz in Fig. 10b.

As the Nyquist frequency approaches $f_{max} = 10$ Hz (Fig. 10a), lower values of GOF score are obtained. Both types of sources provide comparable results in terms of GOF score with the point-source providing a higher score than the extended fault. For $F_{NQ} = 20$ Hz ($= 2 \times f_{max}$), GOF > 9 for all the control points points and all three directions, while for $F_{NQ} = 12.5$ Hz GOF < 8.5 in certain points.

Nevertheless, repeating the same exercise for a different $f_{max} = 6$ Hz, generates higher scores even for a Nyquist frequency of $F_{NQ} = 12.5$ Hz (Fig. 10b). As already expected, this shows that the re-sampling procedure and the Nyquist frequency depend on the targeted maximum frequency that needs to be considered in the FE numerical model.

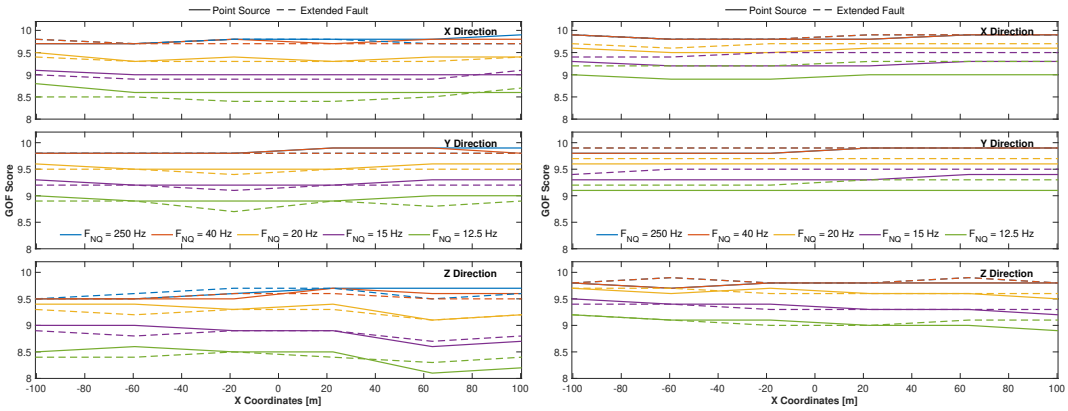

(a) GOF score for an $f_{max} = 10$ Hz. (b) GOF score for an $f_{max} = 6$ Hz.

Figure 10.: Evolution of the GOF score along the AA' cut on the soil surface of the reduced domain.

From a computational point of view, Fig. 11, presents the evolution of CPU time and file size of the input data (in FEM), with respect to the Nyquist frequency defined in the re-sampling approach. As expected, even for the lowest re-sampling value (case 2) the gain on the computation time is around 2.5, while the size of the input files to be read for the FEM solution is divided by 6. These elements maybe do not seem so important referring to the size of the current problem, nevertheless they could be of crucial importance for increasing number of dofs. In order to ensure the quality of the numerical solution, a score of $GOF > 9$ is required everywhere in the domain. As a result, the Nyquist frequency $f_{NQ} = 20$ Hz is chosen for this case as it provides a balance between accuracy of the solution and numerical performance.

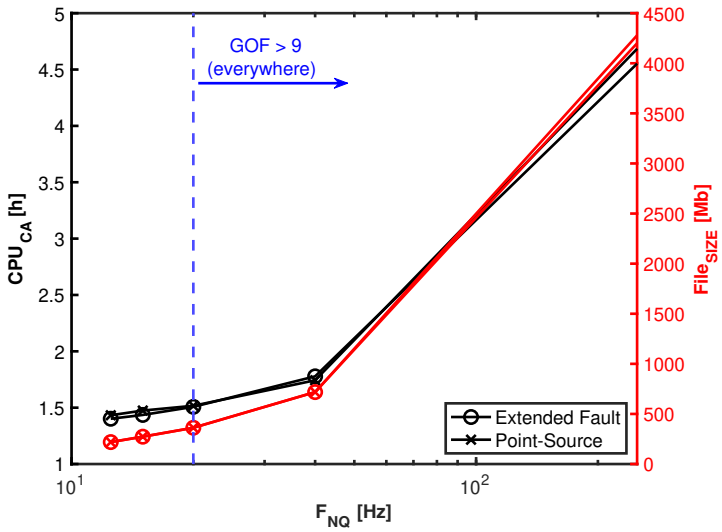

Figure 11.: Evolution of CPU time and file size with respect to the Nyquist frequency.

Consequently, adopting $f_{NQ} = 20$ Hz, the numerical results of the coupling (DRM) are compared to the full-SEM3D wave propagation. Comparison is based on the acceleration time-histories along the AA' line on the soil surface of the reduced domain and presented in Fig. 12a for the point-source and Fig. 12b for the extended fault. A perfect correspondence can be observed between the two signals.

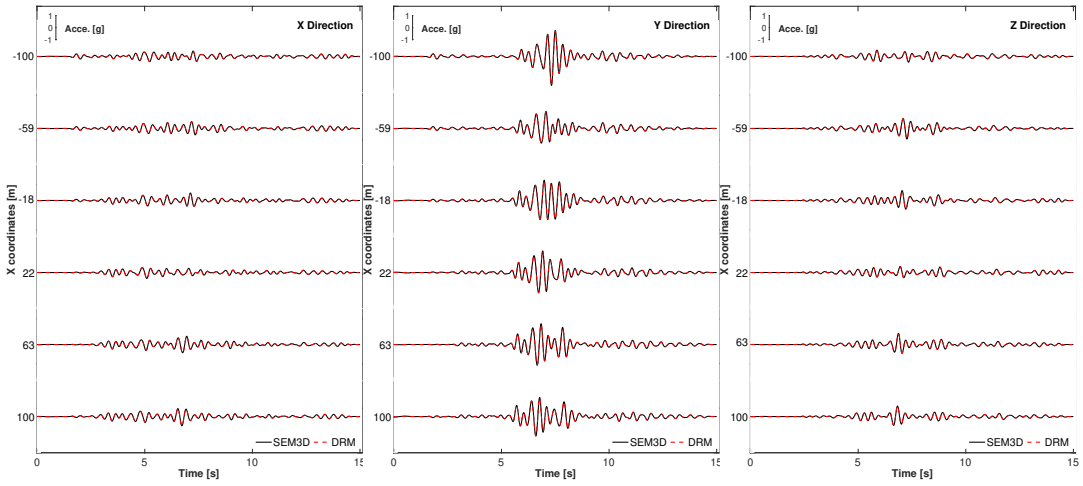

(a) Double-couple point-source.

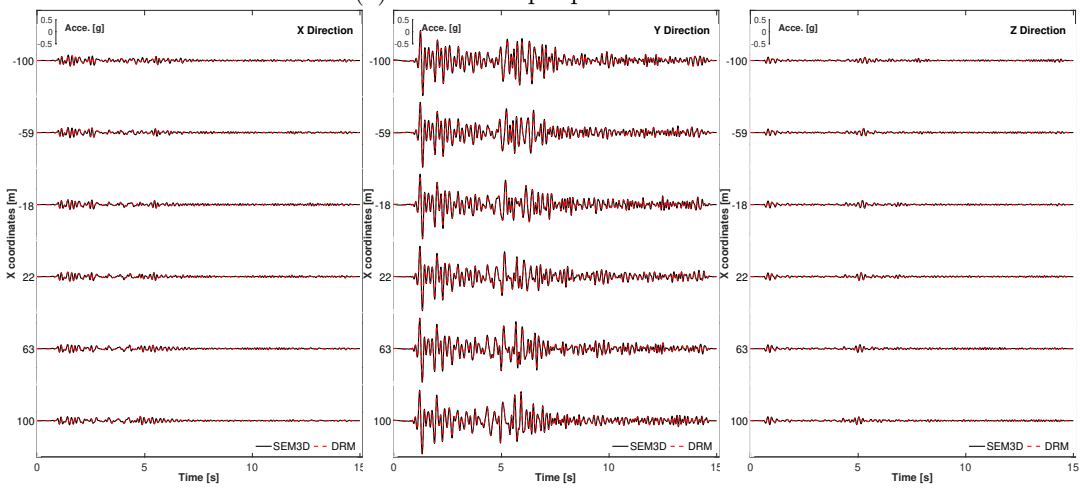

(b) Extended fault.

Figure 12.: Comparison of the acceleration time-histories between the "SEM3D"' solution and the "DRM" approach: X (left), Y (center), and Z (right) component.

4. An application on the Soil-Structure Interaction problem

The proposed methodology is tested here to define the dynamic excitation in a soil-structure interaction (SSI) analysis (Fig. 13). The study focuses at first on the impact of the reduced domain size to be used on the SSI model. Model size in terms of accuracy, and computational efficiency are presented at first in order to evaluate important elements in the coupling procedure. Once the size is fixed, an analysis of structural and site response are provided for the current case.

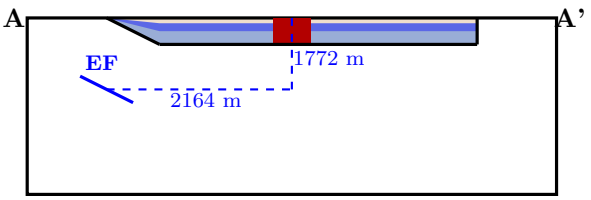

(a) SEM3D model with reduced domain (red square) and the extended fault (EF) excitation.

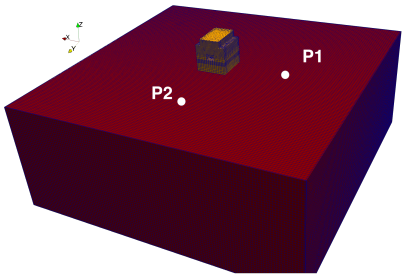

(b) Reduced domain with the structure.

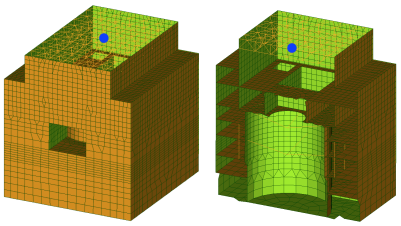

(c) Zoom on the mesh of the structure.

Figure 13.: Representation of the SSI model.

In the following, the geology of the soil domain as well as the dynamic source (extended fault - Fig. 13) are the ones previously described in section 3.1 for the numerical verification of the coupling approach. The considered structure is the Unit 7 reactor building of Kashiwazaki-Kariwa nuclear power plant, as it is a well studied structural model thanks to the OCDE/NERA Karisma benchmark (*85*). For sake of simplicity, shallow foundation is considered and the structure is located on the surface and at the center of the reduced domain. The overall dimensions of the building are (in meters) : $55 \times 55 \times 60$ and it is modeled using beam and shell linear elastic finite elements. For a more detailed description of the building, the reader may refer to e.g. (*25*).

4.1. *Impact of the reduced domain size*

One of the main advantages of the DRM approach being the decrease of the size of the problem in terms of degrees of freedom (DOF), a legitimate question that quickly comes in mind concerns the size to be used for the dimension of the SSI model domain. Several authors have been using the DRM approach to introduce a 3D dynamic excitation on the reduced domain, however in most of these cases, the size of the reduced domain seems to be arbitrarily chosen without any specific justification. One of the most common choices consists of considering the boundary where the forces are applied at a distance that is equal to one time the size of the foundation as it was proposed by (*38*, *58*, *63*) among others. Nevertheless, a starting point of all these studies is the adoption of an elasto-plastic soil behavior with an associated Rayleigh damping for the soil media. In a similar framework, (*57*) considers a reduced domain extending $3 \times \lambda_S$, where λ_S is the larger shear wave length, in the vertical as well as horizontal direction for each side of the model. No material damping is considered in this study.

In the present analysis, three different size models (Fig. 14) for the reduced domain are considered to examine the response of the structure: i) small (200K dofs), ii)

medium (2.8M dofs), and iii) large (7M dofs). The different sizes are chosen as a function of the wavelength $\alpha \times \lambda_S$, where $\lambda_S = 65$ m, and α is a parameter varying for each model. As previously mentioned, (*57*) considers an $\alpha = 3$ for the lateral boundary, while in this study a value of $\alpha = 1, 4, 6.5$ is considered for the small, medium and large model respectively. Vertical size for the medium and large model are fixed at $3 \times \lambda_S$ as in (*57*). Large model is considered the solution of reference, and a comparison is done for the other two model sizes.

As in the numerical verification case, no material damping is considered for the soil layer, which remains linear elastic, and dynamic excitation comes from the extended fault excitation used in the numerical verification approach.

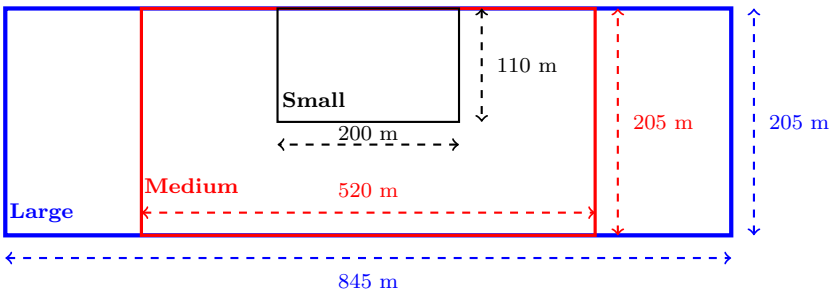

Figure 14.: Different sizes of the reduced domain.

The total prediction residual, Δ, for a given intensity measure (IM) expressed with Eq. 4.1 is used to evaluate the impact of the domain size.

$$\Delta = ln(IM_{REF}) - ln(IM_{SIM}) \tag{4.1}$$

where, $ln(IM_{REF})$ is the natural logarithm of the case of reference (model large), and $ln(IM_{REF})$ the natural logarithm of the simulated one (small or medium). The IM chosen in this case is the 5%-damped response spectral acceleration (PSA) for a point at the top and the base of the structure.

Comparison of the numerical results are presented in Fig. 15, in terms of acceleration time-histories as well as the total residual for the 5%-damped spectral acceleration (Eq. 4.1). Results are examined for a point at the bottom Fig. 15a and 15c and the top of the structure Fig. 15b and 15d. According to this Fig. 15, the small model provides a response that differs from the model of reference while the medium and large domains provide identical results both in the base as well as at the top of the structure. As as a result the medium model size is considered sufficient to represent structural response in this specific framework.

In addition, to represent the "perturbed" soil volume due to the presence of the structure, the GOF criterion is computed for the soil volume and for the three different sizes of the domain. The comparison for the Y component of the excitation is presented in Fig. 16, where it can be seen that in the small domain, the presence of the structure has an important impact on the perturbation of the neighboring soil domain. On the contrary, the medium as well as the large domain provide higher scores closer to the boundary and the perturbation is localized on the center near the structure. As a result, it can be said that the seismic input introduced in the medium and large model is almost equivalent as the diffracted waves from the structure do not impact this zone.

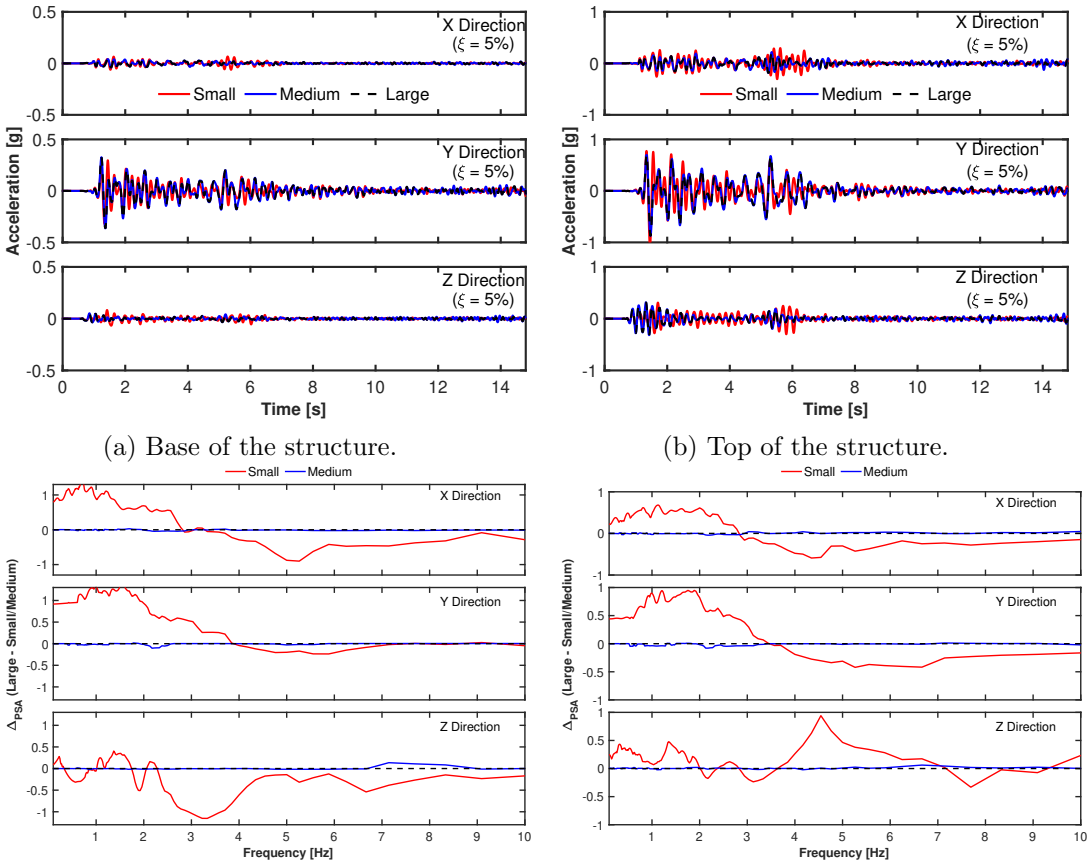

(a) Base of the structure.

(b) Top of the structure.

(c) Base of the structure.

(d) Top of the structure.

Figure 15.: Comparison for different model sizes: acceleration time-histories (top row), and total residual for the 5%-damped spectral acceleration (bottom row).

This last observation also explains why structural response from medium and large models is practically the same.

Consequently, when no material damping is considered in the numerical model, an one-bay width reduced domain is considered insufficient for the description of the structural response. On the contrary, when a boundary-structure distance larger than $4\times\lambda_S$ is considered in each side of the structure, a convergence is observed on structural response. The results hold for the specific framework of the examined case-study.

Finally, in order to bring to surface the importance of the optimization procedure discussed in the previous section and inspired by the work of (*8*), a performance indicator is used based on Eq. 4.2.

$$I = \frac{CPU_{FEM} \cdot File_{SIZE}}{DOF \cdot Memory_{FEM}} \quad \left[\frac{h \cdot Mb}{Mb}\right] \tag{4.2}$$

where CPU_{FEM} is the computational time for the FEM resolution, $File_{SIZE}$ is the size of the transferred data between SEM-FEM, DOF is the degrees-of-freedom of the model, and $Memory_{FEM}$ is the memory used in the FEM model for the resolution.

The idea here is to show the gain in terms of CPU time, memory demand on the FEM computation as well as the size of the input data for a specific size of the problem

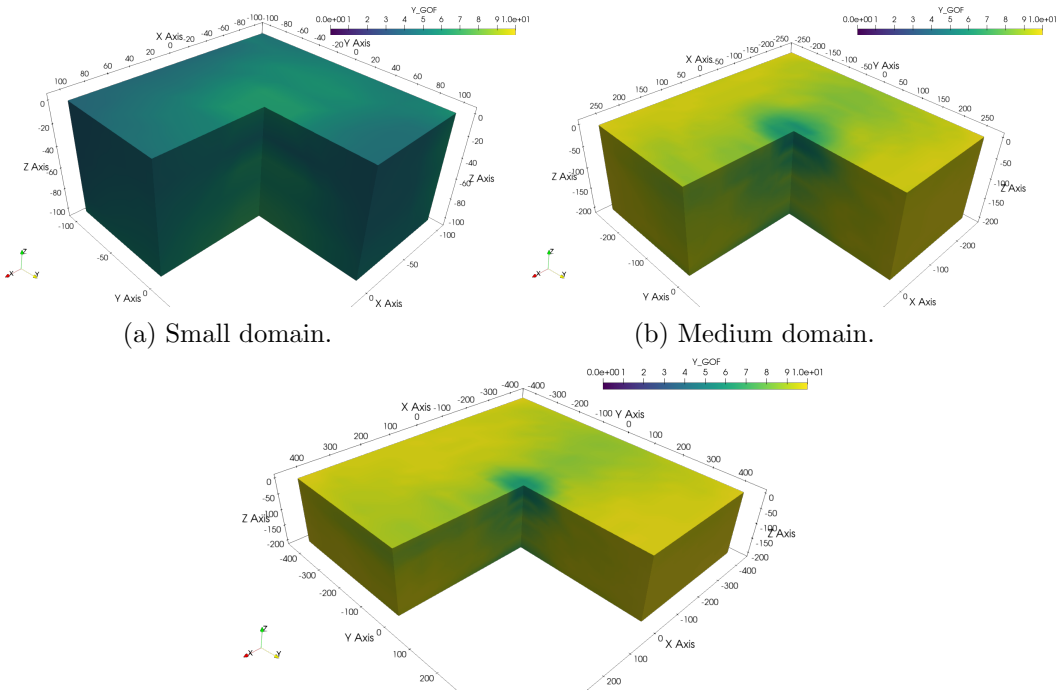

(a) Small domain.

(b) Medium domain.

(c) Large domain.

Figure 16.: GOF score on the soil volume for the 3 sizes of the reduced domain.

in terms of DOFs. The indicator I of Eq. 4.2, is plotted with respect to the evolution of the Nyquist frequency for the different values of F_{NQ} and for the different sizes of the reduced domain model. Results are presented in Fig. 17, for all the cases of the small model (point source - PS, and extended fault - EF) as well as for 4 cases of the medium model and one case for the large model. Two main conclusions can be drawn according to this Fig. 17 : i) an important decrease of the indicator I is observed using the decimation approach ($I_{F_{NQ}=250\,Hz} \approx 10 \cdot I_{F_{NQ}=40\,Hz}$), and ii) for the same decrease in F_{NQ} a coherent impact is observed among the different sizes of the model. For example, $I_{F_{NQ}=40\,Hz} \approx 2 \cdot I_{F_{NQ}=20\,Hz}$ for all three Small-EF/PS, and Medium-EF.

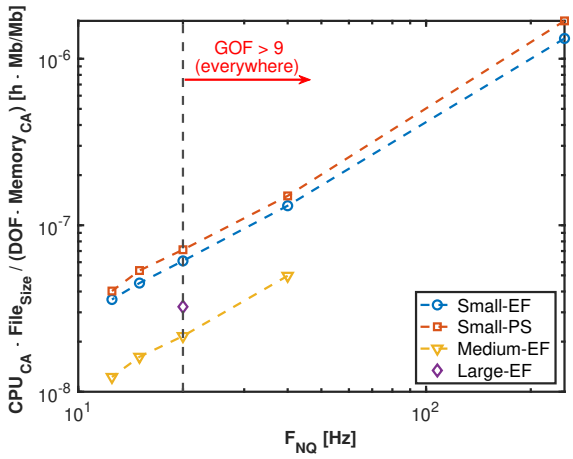

Figure 17.: Performance indicator over the Nyquist frequency.

4.2. *Structure and soil response*

In practice, the most classical way to introduce the dynamic seismic excitation in the SSI problem is the plane wave excitation with vertical incidence (*i.e.* incident wave front is considered homogeneous at the base of the model). In order to highlight the differences of taking into account the complexity of 3D input excitation, the plane wave solution is compared here with the one obtained via the DRM approach.

So as to approximate the plane wave condition from the SEM3D simulation, a borehole condition will be used, for the boundary at the bottom of the reduced domain. With this regard, the incident wave field corresponds to the 3 components of the signal recorded in a unique sensor point located at the center and the base of the reduced domain. In addition, it is supposed that this signal corresponds to a vertically incident plane-wave front at the bottom boundary. Nevertheless, in order to properly define the equivalent response for the borehole boundaries it is necessary to satisfy the radiation condition for the incompatible outgoing (diffracted) waves. Consequently, an absorbing boundary needs to be added following an approach close to the one proposed by (*8*, *12*, *30*). As previously discussed, the paraxial elements, capable to impose the dynamic excitation as well as to absorb the outgoing (diffracted) waves are used in this study. Finally, concerning the lateral boundaries of the finite domain, paraxial elements are used only to absorb outgoing waves diffracted from the structure.

Based on the hypothesis of the previous section, the medium model size ($520 \times 520 \times 205$ m^3 box) is chosen in order to study the SSI in the reduced domain for the extended fault excitation. The impact is examined at first for a point at the top of the structure (blue point in Fig. 13c), and the comparison is made using the prediction residual of Eq. 4.1.

According to Fig. 18, the 3D input excitation introduced via the DRM generates a higher movement than the plane wave excitation ($\Delta_{PSA} > 0$). This is related to the fact that effects of a 3D excitation (e.g directivity effect, surface wave generation) cannot be represented with the simpler plane wave excitation of vertical incidence. Differences are observed in all three directions with higher values observed for the two horizontal X and Y components.

It is well known that one of the most important aspects accounted in a 3D complex excitation is the presence of surface waves. In order to show the presence of these surface waves in the basin and their impact on the level of the structure, Fig. 19a presents an analysis of the velocity motion in Fig. 19a for two different points P1 and P2 (see also Fig. 13b) and the rocking of the building foundation in Fig. 19b.

The surface wave component is “extracted” using the empirical approach proposed by (*86*) which is adopted here. According to this approach, the horizontal (XY plane) velocity time-histories are band-pass filtered for a period of 1-5 s and plotted in Fig. 19a. In addition, rocking is examined here based on the differential displacement computed for two opposite points on the foundation of the structure. This differential displacement is then normalized by the length of the foundation (distance between the two opposite points) and is presented as the rotation angle of the foundation. The same analysis is done along the X and Y axis of the foundation and plotted with respect to time.

It can be observed from Fig 19a that surface waves are present for the dynamic excitation imposed via the DRM approach (i.e. both the incident surface wave and the one induced by the rocking of the structure - solid line in Fig. 19a) and practically absent when the plane wave excitation is used (i.e. only the surface waves generated by the rocking of the structure - dashed line in the Fig. 19a). For the DRM case, the

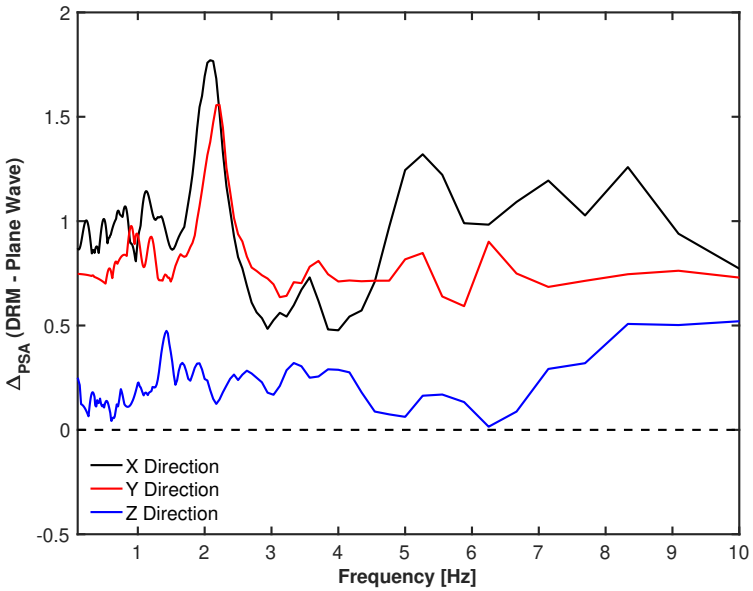

Figure 18.: Response prediction residual for a point at the top of the structure (damping $\xi = 5\%$).

amplitude is more important along the Y component (direction of the excitation) and smaller along the X direction which is related to the presence of the basin.

Similar results are obtained from Fig. 19b, showing that rotation is more important along the Y axis which is the principal direction of the excitation, while a smaller rotation is observed in the X axis which is related to the surface waves generated from the trapezoidal basin. In this case also, the plane wave excitation cannot account for the complexity of a 3D excitation and a weaker rotation is obtained for the structure. The aforementioned results are in accordance with the work of (*46*) that showed that a 3D excitation cannot be replaced by a simple decomposition of the seismic signal in X, Y and Z components.

Finally, a graphical representation of the deformed shape of the model for the DRM excitation is given in Fig. 20 for a time frame at T = 2.4 s, where the displacement field on the reduced domain is presented. For visualization purposes the displacement field is multiplied by a factor of 500 in order to better visualize the movement of the structure and the soil domain. It can be seen from this Fig. 20 that the rocking of the building is mainly in the Y direction, with a smaller displacement along the X component.

5. Conclusion

The numerical analysis of 3D dynamic soil-structure interaction for seismic risk mitigation of important infrastructures such as nuclear power plants, dams and bridges is a quite challenging task that is of crucial importance from an economic and social stand point. Soil topography, characterization of soil geology, and the definition of the dynamic excitation are some of the main sources of uncertainty. In addition, when non-linearity needs to be taken into account, the finite element method consists of the most efficient approach to account for nonlinear behavior. Nevertheless, in the FEM framework, the size of the model in terms of degrees of freedom may rapidly

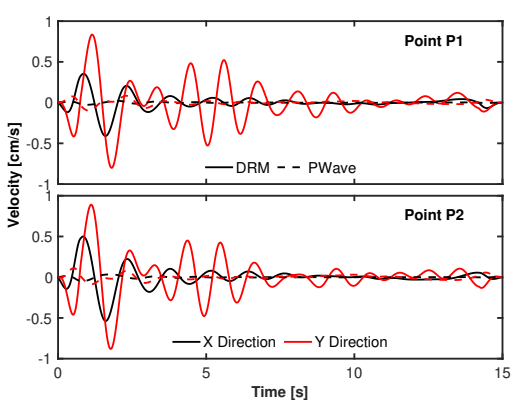

(a) Band-pass filtered (T = 1 - 5 s) velocity field.

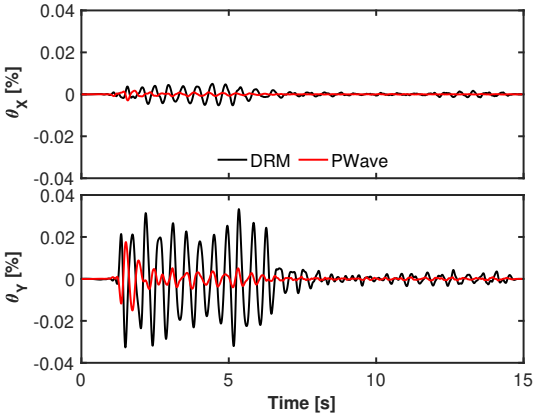

(b) Foundation rocking along the X and Y axis.

Figure 19.: Impact of surface waves on the reduced domain.

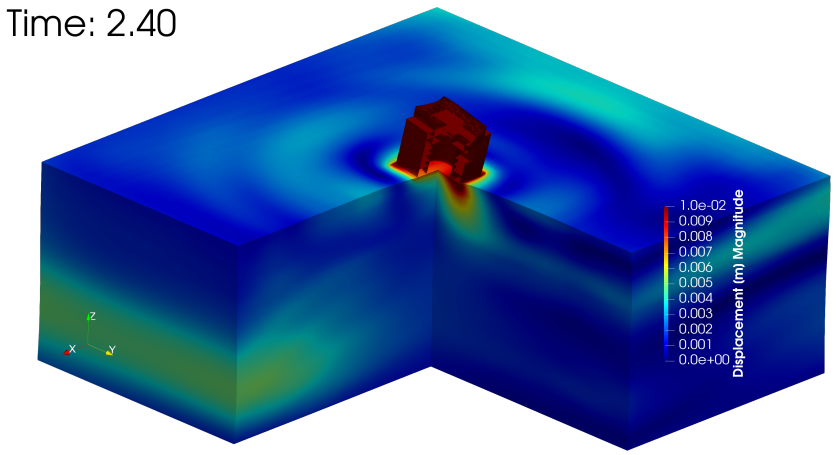

Figure 20.: Deformed shape of the reduced domain (multiplication factor of 500 for visualization purposes).

impact the efficiency of the method, and thus in engineering practice FEM is used in a small/reduced soil domain in order to study 3D nonlinear soil-structure interaction. In this context the dynamic excitation used as an input in FEM solution needs to be a realistic 3D complex wave field, accounting for the: i) complexity of a realistic source, ii) wave propagation path, and iii) local site effects.

In this article, the domain reduction method approach introduced by (*30*), is used in a spectral element method (SEM) - finite element method (FEM) weak coupling in order to ensure the input of a realistic excitation in a FEM framework. The first part of the work focuses on the numerical verification of the SEM-FEM coupling for a canonical case-study with a stratified trapezoidal basin and an increasing complexity of the dynamic excitation source: i) point-source, and ii) extended fault. Considering the different time integration schemes used by the two software, an optimization approach of the transferred kinematic fields is proposed here in order to obtain an equilibrium of accuracy and speed of the numerical solution. The obtained solution based on the proposed optimization approach shows a good correspondence with the solution of reference along with an optimization of the computational cost in terms of CPU time

consumption and memory demand.

In the second part of the work, an application to the soil-structure interaction problem with an extended fault excitation, is presented in order to discuss the impact of the reduced domain size on structural response. In contrast to other published studies, no material or numerical damping is considered in this work. For the linear elastic case, a domain size with lateral boundaries larger than $4 \times \lambda_S$ where λ_S the minimum wavelength inside the domain is considered sufficient to represent accurately the structural response. Once the size is fixed, structural response is examined in order to show the capacity of the SEM-FEM weak coupling to introduce a complex wave-field as an input on the FEM structural model.

The proposed methodology links the 3D physics-based geophysical simulations and the engineering approach of the dynamic analysis of structures. It is a powerful numerical tool, allowing the direct fault-to-structure wave propagation and can be applied in an earthquake-hazard analysis for seismic risk mitigation. This study considers a linear elastic material behavior, with a horizontally stratified soil medium. Nevertheless, from a methodological point of view the proposed SEM-FEM weak coupling can readily incorporate an arbitrary heterogeneous soil geology, and account for a non-linear soil behavior in order to ensure a more realistic site-specific SSI analysis. The aforementioned elements are to be examined in future works by the authors.

Acknowledgment

The authors would like to express their gratitude to the Association Nationale de la Recherche et de la Technologie (ANRT) for their financial support. In addition, a part of the research reported in this paper has been supported by by both the SIGMA-2 project (funded by EDF) and the SEISM Paris Saclay Research Institute (http://www.institut-seism.fr).

References

(1) Berge-Thierry, C.; Voldoire, F.; Ragueneau, F.; Lopez-Caballero, F.; Le Maoult, A. Main Achievements of the Multidisciplinary SINAPS@ Research Project: Towards an Integrated Approach to Perform Seismic Safety Analysis of Nuclear Facilities, *Pure and Applied Geophysics* **2020**, *177* (5), 2299–2351. https://doi.org/10.1007/s00024-019-02194-4.

(2) Poursartip, B.; Fathi, A.; Tassoulas, J.L. Large-scale simulation of seismic wave motion: A review, *Soil Dynamics and Earthquake Engineering* **2020**, *129*, 105909. https://www.sciencedirect.com/science/article/pii/S0267726118314386.

(3) Rodgers, A.J.; Pitarka, A.; Petersson, N.A.; Sjogreen, B.; Pankajakshan, R. GPU-Based Simulation of Earthquake Ground Motions in the San Francisco Bay Area: Path and Site Effects from Suites of Ruptures and Evaluation of the USGS 3D Model with Moderate Magnitude Earthquakes, In *AGU Fall Meeting Abstracts*, 2019; pp S31C–0519.

(4) Castro-Cruz, D.; Gatti, F.; Lopez-Caballero, F. High-fidelity broad-band prediction of regional seismic response: a hybrid coupling of Physics-Based synthetic simulation and Empirical Green's functions, *Natural Hazards* **2020, In Press**.

(5) Faccioli, E.; Maggio, F.; Paolucci, R.; Quarteroni, A. 2D and 3D elastic wave propagation by a pseudo-spectral domain decomposition method, *Journal of Seismology* **1997**, *1* (3), 237–251.

(6) Pitarka, A. Strong Ground Motion Simulations of the M7.1 Kumamoto, Japan Earthquake Using Characterized Heterogeneous Source Models, *Technical Report: Lawrence*

Livermore National Lab. (LLNL), Livermore, CA (United States) **2018**. https://www.osti.gov/biblio/1430931.

(7) Ichimura, T.; Fujita, K.; Yoshiyuki, A.; Quinay, P.E.; Hori, M.; Sakanoue, T. Performance enhancement of three-dimensional soil structure model via optimization for estimating seismic behavior of buried pipelines, *Journal of Earthquake and Tsunami* **2017**, *11* (05), 1750019.

(8) McCallen, D.; Petersson, A.; Rodgers, A.; Pitarka, A.; Miah, M.; Petrone, F.; Sjogreen, B.; Abrahamson, N.; Tang, H. EQSIM—A multidisciplinary framework for fault-to-structure earthquake simulations on exascale computers part I: Computational models and workflow, *Earthquake Spectra* **2020**.

(9) McCallen, D.; Petrone, F.; Miah, M.; Pitarka, A.; Rodgers, A.; Abrahamson, N. EQSIM—A multidisciplinary framework for fault-to-structure earthquake simulations on exascale computers, part II: Regional simulations of building response, *Earthquake Spectra* **2020**.

(10) Zhang, W.; Taciroglu, E. 3D time-domain nonlinear analysis of soil-structure systems subjected to obliquely incident SV waves in layered soil media, *Earthquake Engineering & Structural Dynamics* **2021**, *50* (8), 2156–2173. https://onlinelibrary.wiley.com/doi/abs/10.1002/eqe.3443.

(11) Zhang, W.; Restrepo, D.; Crempien, J.; Erkmen, B.; Taborda, R.; Kurtuluş, A.; Taciroglu, E. A computational workflow for rupture-to-structural-response simulation and its application to Istanbul, *Earthquake Engineering & Structural Dynamics* **2020**, *50*, 1–20.

(12) Bielak, J.; Christiano, P. On the effective seismic input for non-linear soil-structure interaction systems, *Earthquake Engineering & Structural Dynamics* **1984**, *12* (1), 107–119.

(13) Festa, G.; Vilotte, J.P. The Newmark scheme as velocity–stress time-staggering: an efficient PML implementation for spectral element simulations of elastodynamics, *Geophysical Journal International* **2005**, *161* (3), 789–812. https://doi.org/10.1111/j.1365-246X.2005.02601.x.

(14) Léger, P.; Boughoufalah, M. Earthquake input mechanisms for time-domain analysis of dam—foundation systems, *Engineering Structures* **1989**, *11* (1), 37–46. https://linkinghub.elsevier.com/retrieve/pii/014102968990031X.

(15) Tarantola, A. *Inverse problem theory and methods for model parameter estimation*; Society for Industrial and Applied Mathematics: Philadelphia, PA, 2005; OCLC: ocm56672375.

(16) Bradley, B.A.; Pettinga, D.; Baker, J.W.; Fraser, J. Guidance on the utilization of earthquake-induced ground motion simulations in engineering practice, *Earthquake Spectra* **2017**, *33* (3), 809–835.

(17) Pecker, A.; Paolucci, R.; Chatzigogos, C.; Correia, A.; Figini, R. The role of non-linear dynamic soil-foundation interaction on the seismic response of structures, *Bulletin of Earthquake Engineering* **2014**, *12* (3), 1157–1176.

(18) Babuska, I.; Oden, J. Verification and validation in computational engineering and science: basic concepts, *Computer Methods in Applied Mechanics and Engineering* **2004**, *193* (36), 4057–4066. https://www.sciencedirect.com/science/article/pii/S0045782504001781.

(19) Fardis, M.; Carvalho, E.; Elnashai, A.; Faccioli, E.; Pinto, P.; Plumier, A. *Designers' Guide to EN 1998-1 and 1998-5. Eurocode 8: Design Provisions for Earthquake Resistant Structures*; Thomas Telford Publishing, 2005.

(20) Ghaemian, M.; Noorzad, A.; Mohammadnezhad, H. Assessment of Foundation Mass and Earthquake Input Mechanism Effect on Dam–Reservoir–Foundation System Response, *International Journal of Civil Engineering* **2019**, *17* (4), 473–480.

(21) Sotoudeh, P.; Ghaemian, M.; Mohammadnezhad, H. Seismic analysis of reservoir-gravity dam-massed layered foundation system due to vertically propagating earthquake, *Soil Dynamics and Earthquake Engineering* **2019**, *116*, 174–184. https://www.sciencedirect.com/science/article/pii/S0267726118304883.

(22) Zienkiewicz, O.C.; Bicanic, N.; Shen, F.Q. Earthquake Input Definition and the

Trasmitting Boundary Conditions. In *Advances in Computational Nonlinear Mechanics*; Doltsinis, I.S., Ed.; Springer Vienna: Vienna, 1989; pp 109–138. http://link.springer.com/10.1007/978-3-7091-2828-2_3.

(23) Gajan, S.; Raychowdhury, P.; Hutchinson, T.C.; Kutter, B.L.; Stewart, J.P. Application and validation of practical tools for nonlinear soil-foundation interaction analysis, *Earthquake Spectra* **2010**, *26* (1), 111–129.

(24) Devésa, G.; Guyonvarh, V. Use of coupled and regulatory method in Soil-Structure Interaction and Soil-Fluid-Structure Interaction for nuclear plants and dams, In *First European Conference on Earthquake Engineering and Seismology*, Geneva, 2006; pp 3–8.

(25) Alves Fernandes, V.A.; Banci, F.; Devesa, G.; Greffet, N.; Jacquet, M.; Kham, M.; Nieto-Ferro, A.; Voldoire, F.; Zentner, I. Dynamic soil-structure interaction modeling strategies applied to Kashiwazaki-Kariwa nuclear power plant case-study, *COMPDYN 2017 - Proceedings of the 6th International Conference on Computational Methods in Structural Dynamics and Earthquake Engineering* **2017**, *1* (June), 2330–2342.

(26) Nieto Ferro, A.; Clouteau, D.; Greffet, N.; Devésa, G. On a hybrid Laplace-time domain approach to dynamic interaction problems, *European Journal of Computational Mechanics* **2012**, *21* (3-6), 290–299.

(27) Gatti, F.; Touhami, S.; Lopez-Caballero, F.; Paolucci, R.; Clouteau, D.; Fernandes, V.A.; Kham, M.; Voldoire, F. Broad-band 3-D earthquake simulation at nuclear site by an all-embracing source-to-structure approach, *Soil Dynamics and Earthquake Engineering* **2018**, *115*, 263–280.

(28) Abell, J.A.; Orbović, N.; McCallen, D.B.; Jeremic, B. Earthquake soil-structure interaction of nuclear power plants, differences in response to 3D, 3× 1D, and 1D excitations, *Earthquake Engineering & Structural Dynamics* **2018**, *47* (6), 1478–1495.

(29) Dello Russo, A.; Sica, S.; Del Gaudio, S.; De Matteis, R.; Zollo, A. Near-source effects on the ground motion occurred at the Conza Dam site (Italy) during the 1980 Irpinia earthquake, *Bulletin of Earthquake Engineering* **2017**, *15* (10), 4009–4037.

(30) Bielak, J.; Yoshimura, C.; Hisada, Y.; Fernández, A. Domain Reduction Method for Three-Dimensional Earthquake Modeling in Localized Regions, Part I: Theory, *Bulletin of the Seismological Society of America* **2003**, *93* (2), 825–840.

(31) De Martin, F.; Modaressi, H.; Aochi, H. Coupling of FDM and FEM in seismic wave propagation, In *4th International Conference on Earthquake Geotechnical Engineering*, Thessaloniki, Greece, June, 2007; https://hal-brgm.archives-ouvertes.fr/hal-00560540.

(32) Quinay, P.E.B.; Ichimura, T.; Hori, M.; Nishida, A.; Yoshimura, S. Seismic Structural Response Estimates of a Fault-Structure System Model with Fine Resolution Using Multiscale Analysis with Parallel Simulation of Seismic-Wave Propagation, *Bulletin of the Seismological Society of America* **2013**, *103* (3), 2094–2110. Doi: 10.1785/0120120216.

(33) Jeremić, B.; Jie, G.; Preisig, M.; Tafazzoli, N. Time domain simulation of soil–foundation–structure interaction in non-uniform soils, *Earthquake Engineering & Structural Dynamics* **2009**, *38* (5), 699–718.

(34) Kontoe, S.; Zdravkovic, L.; Potts, D. The domain reduction method for dynamic coupled consolidation problems in geotechnical engineering, *International journal for numerical and analytical methods in geomechanics* **2008**, *32* (6), 659–680.

(35) Luo, C.; Lou, M.; Gui, G.; Wang, H. A modified domain reduction method for numerical simulation of wave propagation in localized regions, *Earthquake Engineering and Engineering Vibration* **2019**, *18* (1), 35–52.

(36) Preisig, M.; Jeremic, B. *Nonlinear finite element analysis of dynamic soil-foundation-structure interaction*; Technical Report, 2005.

(37) Solberg, J.M.; Hossain, Q.; Mseis, G. Nonlinear time-domain soil–structure interaction analysis of embedded reactor structures subjected to earthquake loads, *Nuclear Engineering and Design* **2016**, *304*, 100–124.

(38) Wang, H.; Yang, H.; Sinha, S.K.; Luo, C.; Jeremic, B. 3-D Non-Linear Earthquake Soil-Structure Interaction Modeling of Embedded Small Modular Reactor (SMR), In *Proceed-*

ings of the 24th International Conference on Structural Mechanics in Reactor Technology (SMiRT 24)', Busan, South Korea, 2017.

(39) Casadei, F.; Gabellini, E. *Implementation of a 3D Coupled Spectral Element/finite Element Solver for Wave Propagation and Soil-structure Interaction Simulations: Numerical Examples*; Office for Official Publications of the European Communities, 1998.

(40) Zuchowski, L.; Brun, M.; De Martin, F. Co-simulation coupling spectral/finite elements for 3D soil/structure interaction problems, *Comptes Rendus - Mecanique* **2018**, *346* (5), 408–422.

(41) Brun, M.; De Martin, F.; Richart, N. Hybrid asynchronous SEM/FEM co-simulation for seismic nonlinear analysis of concrete gravity dams, *Computers and Structures* **2021**, *245*, 106459. https://doi.org/10.1016/j.compstruc.2020.106459.

(42) Combescure, A.; Gravouil, A. A numerical scheme to couple subdomains with different time-steps for predominantly linear transient analysis, *Computer methods in applied mechanics and engineering* **2002**, *191* (11-12), 1129–1157.

(43) Gravouil, A.; Combescure, A. Multi-time-step explicit–implicit method for non-linear structural dynamics, *International Journal for Numerical Methods in Engineering* **2001**, *50* (1), 199–225.

(44) Bernardi, C.; Debit, N.; Maday, Y. Coupling finite element and spectral methods: First results, *Mathematics of Computation* **1990**, *54* (189), 21–39.

(45) Matsumoto, M.; Arakawa, T.; Kitayama, T.; Mori, F.; Okuda, H.; Furumura, T.; Nakajima, K. Multi-scale coupling simulation of seismic waves and building vibrations using ppOpen-HPC, *Procedia Computer Science* **2015**, *51* (1), 1514–1523. http://dx.doi.org/10.1016/j.procs.2015.05.341.

(46) Abell, J.A.; Orbović, N.; McCallen, D.B.; Jeremić, B. Earthquake soil-structure interaction of nuclear power plants, differences in response to 3-D, 3 1-D, and 1-D excitations, *Earthquake Engineering and Structural Dynamics* **2018**. https://doi.org/10.1002/eqe.3026.

(47) Fu, H.; He, C.; Chen, B.; Yin, Z.; Zhang, Z.; Zhang, W.; Zhang, T.; Xue, W.; Liu, W.; Yin, W.; et al. 18.9-Pflops Nonlinear Earthquake Simulation on Sunway TaihuLight: Enabling Depiction of 18-Hz and 8-Meter Scenarios, *Proceedings of the International Conference for High Performance Computing, Networking, Storage and Analysis, SC 2017* **2017**.

(48) Ichimura, T.; Agata, R.; Hori, T.; Hirahara, K.; Hashimoto, C.; Hori, M.; Fukahata, Y. An elastic/viscoelastic finite element analysis method for crustal deformation using a 3-D island-scale high-fidelity model, *Geophysical Journal International* **2016**, *206* (1), 114–129.

(49) Ichimura, T.; Agata, R.; Hori, T.; Satake, K.; Ando, K.; Baba, T.; Hori, M. Tsunami analysis method with high-fidelity crustal structure and geometry model, *Journal of Earthquake and Tsunami* **2017**, *11* (5), 1–18.

(50) Ichimura, T.; Fujita, K.; Horikoshi, M.; Meadows, L.; Nakajima, K.; Yamaguchi, T.; Koyama, K.; Inoue, H.; Naruse, A.; Katsushima, K.; et al. A fast scalable implicit solver with concentrated computation for nonlinear time-evolution problems on low-order unstructured finite elements, In *2018 IEEE International Parallel and Distributed Processing Symposium (IPDPS)*, IEEE, 2018; pp 620–629.

(51) Komatitsch, D.; Tromp, J. Introduction to the spectral element method for three-dimensional seismic wave propagation, *Geophysical journal international* **1999**, *139* (3), 806–822.

(52) Komatitsch, D.; Vilotte, J.P.; Vai, R.; Castillo-Covarrubias, J.M.; Sánchez-Sesma, F.J. The spectral element method for elastic wave equations—application to 2-D and 3-D seismic problems, *International Journal for numerical methods in engineering* **1999**, *45* (9), 1139–1164.

(53) Cupillard, P.; Delavaud, E.; Burgos, G.; Festa, G.; Vilotte, J.P.; Capdeville, Y.; Montagner, J.P. RegSEM: a versatile code based on the spectral element method to compute seismic wave propagation at the regional scale, *Geophysical Journal International* **2012**, *188* (3), 1203–1220. https://doi.org/10.1111/j.1365-246X.2011.05311.x.

(54) De Basabe, J.D.; Sen, M.K. A comparison of finite-difference and spectral-element methods for elastic wave propagation in media with a fluid-solid interface, *Geophysical Journal International* **2014**, *200* (1), 278–298. https://doi.org/10.1093/gji/ggu389.

(55) Lax, P.D.; Wendroff, B. Difference schemes for hyperbolic equations with high order of accuracy, *Communications on Pure and Applied Mathematics* **1964**, *17* (3), 381–398. https://onlinelibrary.wiley.com/doi/abs/10.1002/cpa.3160170311.

(56) Maday, Y.; Patera, A.T. Spectral element methods for the incompressible Navier-Stokes equations, In *IN: State-of-the-art surveys on computational mechanics (A90-47176 21-64). New York, American Society of Mechanical Engineers, 1989, p. 71-143. Research supported by DARPA.*, 1989; pp 71–143.

(57) Poursartip, B.; Fathi, A.; Kallivokas, L.F. Seismic wave amplification by topographic features: A parametric study, *Soil Dynamics and Earthquake Engineering* **2017**, *92*, 503–527. https://www.sciencedirect.com/science/article/pii/S0267726116304559.

(58) Sinha, S.K.; Feng, Y.; Yang, H.; Wang, H.; Jeremic, B. 3-d non-linear modeling and its effects in earthquake soil-structure interaction, In *Proceedings of the 24th International Conference on Structural Mechanics in Reactor Technology (SMiRT 24)', Busan, South Korea*, 2017.

(59) Wang, H.; Yang, H.; Sinha, S.K.; Luo, C.; Jeremic, B. 3D non-linear earthquake soil-structure interaction modeling of embedded small modular reactor (SMR), In *Proceedings of the 24th International Conference on Structural Mechanics in Reactor Technology (SMiRT 24)', Busan, South Korea*, 2017.

(60) Clayton, R.; Engquist, B. Absorbing boundary conditions for acoustic and elastic wave equations, *Bulletin of the seismological society of America* **1977**, *67* (6), 1529–1540.

(61) Engquist, B.; Majda, A. Absorbing boundary conditions for the numerical simulation of waves, *Math. Comput* **1977**, *31*, 629–651.

(62) Modaressi, H.; Benzenati, I. Paraxial approximation for poroelastic media, *Soil Dynamics and Earthquake Engineering* **1994**, *13* (2), 117–129.

(63) Wu, S.; Eckert, E.; Huang, J.; Mccallen, D. *Evaluation of the Domain Reduction Method applied to broad-band, near-fault earthquake ground motions with inter-code comparisons*; Technical Report; 07, 2020.

(64) Herrera, I.; Bielak, J. Soil-structure interaction as a diffraction problem, In *Proceedings of the 6th World Conference on Earthquake Engineering. New Delhi, India*, 1977; Vol. 2, pp 1467–1472.

(65) Yoshimura, C.; Bielak, J.; Hisada, Y.; Fernández, A. Domain reduction method for three-dimensional earthquake modeling in localized regions, part II: Verification and applications, *Bulletin of the seismological Society of America* **2003**, *93* (2), 825–841.

(66) Petropoulos, G. Soil-Structure Interaction Analysis Using High-Performance Parallel Computation, *Thesis* **2008**, *44*.

(67) Semblat, J.F.; Lenti, L.; Gandomzadeh, A. A simple multi-directional absorbing layer method to simulate elastic wave propagation in unbounded domains, *International Journal for Numerical Methods in Engineering* **2011**, *85* (12), 1543–1563. https://onlinelibrary.wiley.com/doi/abs/10.1002/nme.3035.

(68) Poursartip, B.; Kallivokas, L.F. Model dimensionality effects on the amplification of seismic waves, *Soil Dynamics and Earthquake Engineering* **2018**, *113* (July), 572–592.

(69) Cremonini, M.G.; Christiano, P.; Bielak, J. Implementation of effective seismic input for soil-structure interaction systems, *Earthquake Engineering & Structural Dynamics* **1988**, *16* (4), 615–625. https://onlinelibrary.wiley.com/doi/abs/10.1002/eqe.4290160411.

(70) Code_Aster. *General public licensed structural mechanics finite element software, included in the Salomé-Méca simulation platform. Website http://www.code-aster.org. En particulier : [R4.02.05] Éléments de frontière absorbante*; Technical Report, 2017.

(71) Bamberger, A.; Engquist, B.; Halpern, L.; Joly, P. Higher Order Paraxial Wave Equation Approximations in Heterogeneous Media, *SIAM Journal on Applied Mathematics* **1988**,

48 (1), 129–154. http://www.jstor.org/stable/2101501.

(72) MED. "MEDCoupling developer's guide", SALOME-platform, [Online] Available: http://docs.salome-platform.org/latest/dev/MEDCoupling/developer/index.html, [Accessed 17 04 2020], 2019.

(73) Komatitsch, D.; Tromp, J. Introduction to the spectral element method for three-dimensional seismic wave propagation, *Geophysical Journal International* **1999**, *139* (3), 806–822.

(74) Seriani, G.; Priolo, E. Spectral element method for acoustic wave simulation in heterogeneous media, *Finite Elements in Analysis and Design* **1994**, *16* (3-4), 337–348.

(75) Watanabe, K.; Pisanò, F.; Jeremić, B. Discretization effects in the finite element simulation of seismic waves in elastic and elastic-plastic media, *Engineering with Computers* **2017**, *33* (3), 519–545.

(76) Zhang, L.; Wang, J.T.; Xu, Y.J.; He, C.H.; Zhang, C.H. A procedure for 3D seismic simulation from rupture to structures by coupling SEM and FEM, *Bulletin of the Seismological Society of America* **2020**, *110* (3), 1134–1148.

(77) Code_Aster. General public licensed structural mechanics finite element software, included in the Salomé-Méca simulation platform. Website http://www.code-aster.org. **2017**.

(78) Kristeková, M.; Kristek, J.; Moczo, P. Time-frequency misfit and goodness-of-fit criteria for quantitative comparison of time signals, *Geophysical Journal International* **2009**, *178* (2), 813–825.

(79) Kristeková, M.; Kristek, J.; Moczo, P.; Day, S.M. Misfit criteria for quantitative comparison of seismograms, *Bulletin of the seismological Society of America* **2006**, *96* (5), 1836–1850.

(80) Anderson, J.G. Quantitative measure of the goodness-of-fit of synthetic seismograms, In *13th world conference on earthquake engineering conference proceedings, Vancouver, Canada, Paper*, Vancouver, B.C., Canada, 2004; http://www.iitk.ac.in/nicee/wcee/article/13{_}243.pdf.

(81) Chaljub, E.; Maufroy, E.; Moczo, P.; Kristek, J.; Hollender, F.; Bard, P.Y.; Priolo, E.; Klin, P.; De Martin, F.; Zhang, Z.; et al. 3-D numerical simulations of earthquake ground motion in sedimentary basins: testing accuracy through stringent models, *Geophysical Journal International* **2015**, *201* (1), 90–111.

(82) Hollender, F.; Manakou, M.; Bard, P.; Chaljub, E.; Raptakis, D.; Pitilakis, K.; Tsuno, S. Euroseistest verification and validation project: an international effort to evaluate ground motion numerical simulation relevance, *Seism. Res. Lett.* **2010**, *81*, 322.

(83) Berenger, J.P.; et al. A perfectly matched layer for the absorption of electromagnetic waves, *Journal of computational physics* **1994**, *114* (2), 185–200.

(84) Ide, S. Complex source processes and the interaction of moderate earthquakes during the earthquake swarm in the Hida-Mountains, Japan, 1998, *Tectonophysics* **2001**, *334* (1), 35–54.

(85) *Review of Seismic Evaluation Methodologies for Nuclear Power Plants Based on a Benchmark Exercise*; TECDOC Series 1722; International Atomic Energy Agency: Vienna, 2014; https://www.iaea.org/publications/10580/review-of-seismic-evaluation-methodologies-for-nuclear-power-plants-based-on-a-benchmark-exercise.

(86) Miura, H.; Okamura, T.; Matsuoka, M.; Leal, M.; García, H.; Pulido, N. Empirical Models for Surface-and Body-Wave Amplifications of Response Spectra in the Bogotá Basin, Colombia, *Bulletin of the Seismological Society of America* **2019**, *109* (3), 987–1004.